Accepted by ApJ
Preprint typeset using LaTeX style emulateapj v. 5/2/11

arXiv:1510.08049v4 [astro-ph.HE] 31 Jul 2016

ANALYZING THE LARGEST SPECTROSCOPIC DATASET OF STRIPPED SUPERNOVAE TO IMPROVE THEIR IDENTIFICATIONS AND CONSTRAIN THEIR PROGENITORS

Yu-Qian Liu[1], Maryam Modjaz[1], Federica B. Bianco[1,2], Or Graur[1,3]

Accepted by ApJ

ABSTRACT

Using the largest spectroscopic dataset of stripped-envelope core-collapse supernovae (stripped SNe), we present a systematic investigation of spectral properties of Type IIb SNe (SNe IIb), Type Ib SNe (SNe Ib), and Type Ic SNe (SNe Ic). Prior studies have been based on individual objects or small samples. Here, we analyze 242 spectra of 14 SNe IIb, 262 spectra of 21 SNe Ib, and 207 spectra of 17 SNe Ic based on the stripped SN dataset of Modjaz et al. (2014) and other published spectra of individual SNe. Each SN in our sample has a secure spectroscopic ID, a date of V-band maximum light, and most have multiple spectra at different phases. We analyze these spectra as a function of subtype and phase in order to improve the SN identification scheme and constrain the progenitors of different kinds of stripped SNe. By comparing spectra of SNe IIb with those of SNe Ib, we find that the strength of Hα can be used to quantitatively differentiate between these two subtypes at all epochs. Moreover, we find a continuum in observational properties between SNe IIb and Ib. We address the question of hidden He in SNe Ic by comparing our observations with predictions from various models that either include hidden He or in which He has been burnt. Our results favor the He-free progenitor models for SNe Ic. Finally, we construct continuum-divided average spectra as a function of subtype and phase to quantify the spectral diversity of the different types of stripped SNe.

Subject headings: supernovae: general—supernovae: individual (SNe 1993J, 1998dt, 1999ex, 2005bf, 2005E, 2006el, 2007Y, 2009mg, 2011dh, 2011ei)—methods: data analysis

1. INTRODUCTION

Supernovae (SNe) mark the diverse deaths of stars and contribute to the production and release of heavy elements in the universe. In particular, stripped-envelope core-collapse SNe (stripped SNe; e.g., Clocchiatti et al. 1997; Filippenko 1997; Modjaz et al. 2014) are the deaths of massive stars ($\gtrsim 8$ M$_\odot$) that have lost some, if not all, of their outer hydrogen and helium envelopes through strong winds (Woosley et al. 1993), binary interactions (Nomoto et al. 1995; Podsiadlowski et al. 2004), or enhanced mixing (Frey et al. 2013). Unlike Type II SNe (SNe II), whose spectra show strong H lines during all photospheric phases, stripped SNe have spectra with no or weak H lines, or strong H lines only at early phases. In contrast to Type Ia SNe (SNe Ia), which are considered to be the outcome of thermonuclear explosions of carbon-oxygen white dwarfs (Nugent et al. 2011; Bloom et al. 2012; Maoz et al. 2014), stripped SNe are thought to explode due to the core-collapse of their massive progenitors ($\gtrsim 8$ M$_\odot$; Woosley et al. 2002; Burrows 2013). Following the empirical classification based on the presence or absence of certain lines in SN spectra (Filippenko 1997), stripped SNe can be divided into several subtypes: Type IIb SNe (SNe IIb) initially show strong H lines, but over time the H lines become weaker whereas the He I lines grow stronger (Filippenko et al. 1993); Type Ib SNe (SNe Ib), which show conspicuous He I lines; Type Ic SNe (SNe Ic), which do not show prominent H lines or He I lines; and broad-lined SNe Ic (SNe Ic-bl), which are similar to SNe Ic, but exhibit much broader lines (by ~ 9000 km s^{-1} around maximum light; Modjaz et al. 2015).

Dozens of stripped SNe are discovered every year, but only a few of them have a large amount of spectroscopic and photometric data and have been studied in detail. For example, the best-studied SN IIb and SN Ic are SN 1993J (Filippenko et al. 1993; Matheson et al. 2000a,b) and SN 1994I (Filippenko et al. 1995; Richmond et al. 1996), respectively. However, statistical analyses of large SN samples are needed to characterize spectra of different SN subtypes. This will help to explore whether there is an observational continuum between SN subtypes, as well as to correctly classify SNe, which is vital in matching various progenitor models to different SN subtypes. In addition, it will help to sharpen the use of SNe Ia for high-precision cosmology since SNe Ic, which are potential contaminants in high-redshift SN Ia surveys (e.g., Clocchiatti 2000; Homeier 2005; Graur & Maoz 2013; Jones et al. 2013; Rodney et al. 2015), can be better distinguished. Finally, statistical studies will help to assess whether there is hidden He in SN Ic spectra via comparisons between the bulk properties of observed spectra and predicted spectroscopic properties based on various models. The most recent work that statistically compared spectra of different stripped SN subtypes was conducted by Matheson et al. (2001), who used 84 spectra of 28 stripped SNe, many of which did not have light curves to determine the phases of the spectra. We discuss this paper in detail in Sections 4.4 and 5.2.1.

Recently, Modjaz et al. (2014) published optical

[1] Center for Cosmology and Particle Physics, New York University, 4 Washington Place, New York, NY 10003-6603, USA; YL1260@nyu.edu
[2] Center for Urban Science and Progress, New York University, 1 MetroTech Center, Brooklyn, NY 11201, USA
[3] Department of Astrophysics, American Museum of Natural History, Central Park West and 79th Street, New York, NY 10024-5192, USA

spectra of 73 stripped SNe collected at the Harvard-Smithsonian Center for Astrophysics (CfA; the M14 sample hereafter), doubling the supply of well-observed stripped SNe. Forty-four of these 73 stripped SNe have a date of maximum light. Besides the above data, which comprise more than half of our SN sample, we have collected the spectra of all available stripped SNe from the literature until September of 2014. Thus, we analyze the optical spectra of a sample of 71 stripped SNe with a well-defined date of maximum light and type.

This study will focus on spectroscopic comparisons between SNe IIb, SNe Ib, and SNe Ic. A spectroscopic comparison between SNe Ic, SNe Ic-bl without Gamma-Ray Bursts (GRBs), and SNe Ic-bl connected with GRBs is presented in a companion paper (Modjaz et al. 2015). In Section 2, we summarize the phases and references of the SN spectral sample used in this paper. In Section 3, we describe the velocity and strength measurements we make based on the SN spectra. In Section 4, we conduct spectroscopic comparisons between SNe IIb and SNe Ib to see whether there is an observational continuum between the two subtypes, as well as to better characterize them. In Section 5, we discuss whether there is hidden He in progenitors of SNe Ic using the strength and velocity of the O I λ7774 line and the velocity of the Fe II λ5169 line as indicators to test two competing models. We also explore the spectral diversity within each SN subtype using mean spectra and their corresponding standard deviations in Section 6. Finally, we summarize our conclusions in Section 7.

2. SN SPECTRAL SAMPLES

We list our SN IIb and Ib samples in Tables 1 and 2, respectively. Our SN Ic sample is the same as in Modjaz et al. (2015). To improve both the accuracy and the precision of our analyses, we consistently use the date of maximum light in the V-band since it is the best-sampled light curve for current SN photometric datasets (Bianco et al. 2014). For SNe with V-band light curves in the literature but for which the authors did not explicitly report the date of maximum light (e.g., SN 2004ff; Drout et al. 2011), we calculated the date of V-band maximum using a polynomial fit as described in Bianco et al. (2014). For SNe without V-band light curves but with a date of maximum light in either the R-band or B-band (e.g., SN 1998fa; Matheson et al. 2001), we converted the known date to the date of V-band maximum light using the relationship listed in Bianco et al. (2014): $\mathrm{JD}_{Vmax} = \mathrm{JD}_{Rmax} - 1.8$ days $= \mathrm{JD}_{Bmax} + 2.3$ days, where JD stands for Julian date.

Since we want to analyze SN spectra as a function of SN type and phase in a statistical manner, we included as many stripped SNe that have a secure ID and a date of maximum light as possible. The classifications of these SNe are taken from the literature as indicated in Tables 1 and 2. Authors usually classifies a SN using SNID, GELATO, or other SN classification codes. Note that we adopt the changes in classification as discussed in Modjaz et al. (2014). We only include normal SNe IIb, SNe Ib and SNe Ic, i.e., we exclude SNe Ib-n (e.g., SN 2006jc; Pastorello et al. 2007; Modjaz et al. 2014) , SNe Ib-pec (e.g., SNe 2002bj, 2007uy, and 2009er; Poznanski et al. 2010; Modjaz et al. 2014), SNe Ib-Ca (e.g., SN 2005E; Perets et al. 2010), super-luminous SNe Ic (e.g., SN 2010gx; Quimby et al. 2011; Stoll et al. 2011; Gal-Yam 2012), and SNe that transition from one type to another during their evolution (e.g., ASASSN-15ed; Pastorello et al. 2015). Our SN spectroscopic sample consists of relevant spectra (that satisfy the above requirements) in the database templates-2.0 of the SuperNova IDentification code (SNID;[4] Blondin & Tonry 2007), the M14 sample, and relevant spectra from the literature available before September of 2014. These spectra were drawn from SNID, public archives such as the CfA Supernova Archive[5] and Weizmann Interactive Supernova data REPository (WISeREP;[6] Yaron & Gal-Yam 2012), or requested from the authors.

In summary, we have 242 optical spectra of 14 SNe IIb, 262 optical spectra of 21 SNe Ib, and 207 optical spectra of 17 SNe Ic. These SNe have low redshifts ($z < 0.027$) with mean and median values of 0.011 and 0.009, respectively.

3. SPECTRAL ANALYSIS METHODS

We used two spectral analysis methods that are the same as those in Modjaz et al. (2015). One is constructing average spectra using the whole spectra, as explained in detail in Section 3.1. We used them to directly compare spectra in Sections 4.1 and 5.1, and to quantify the spectral diversity of different subtypes of SNe in Section 6. The other method is to quantify spectral features based on individual lines by measuring their absorption velocities and strengths. We analyzed these measurements in a statistical way, i.e., constructing error bars and average values of the measurements, to conduct a spectroscopic comparison between SNe IIb and SNe Ib in Sections 4.2–4.6 and to constrain progenitors of SNe Ic in Section 5.2.

Before analyzing the spectra, we pre-process them, as discussed in detail in Appendix A. In particular, we would like to remove the effect of different dispersions and wavelength ranges due to the use of different telescopes, as well as reddening of the spectra. The spectra in our sample are flattened via the same procedure used to prepare the spectra for SNID, thus the resultant spectra (i.e., SNID templates) have the same format as those in the SNID database templates-2.0. Then we used the SNID templates we constructed above, as well as the SNID templates of stripped SNe that are already in the SNID database templates-2.0, to construct mean spectra (Section 3.1). In order to quantify SN features, we measure their absorption velocities and strengths (Section 3.2). The corresponding error bars were produced using the uncertainty arrays of spectra (Appendix B) and Monte Carlo (MC) simulations (Section 3.3). In order to explore bulk properties as a function of different Stripped SN subtypes, we calculated a rolling weighted average of the measurements (Appendix D).

All of the mean spectra, the new SNID templates, and the code that produces uncertainty arrays of spectra are published under DOI 10.5281/zenodo.58766 and DOI 10.5281/zenodo.58767. They are available on our SNYU github website, [7] and also linked from our SNYU

[4] http://people.lam.fr/blondin.stephane/software/snid/index.html
[5] http://www.cfa.harvard.edu/supernova/SNarchive.html
[6] http://wiserep.weizmann.ac.il/spectra/list
[7] https://github.com/nyusngroup

Table 1
Spectral sample of SNe IIb

SN Name	Phases[a] of Spectra	References[b]
SN 1993J	−18, −18, −17, −16, −11, −5, −4, −3, −2, −2, −2, 1, 3, 3, 4, 4, 5, 6, 7, 11, 12, 13, 17, 20, 24, 29, 30, 32, 35, 35, 36, 36, 37, 38, 39, 62, 64, 68, 70, 72, 88, 90+(32)	SNID (J94, B95, M00, F05), M14
SN 1996cb	−20, −19, −4, −1, 3, 4, 5, 6, 25, 27, 31, 35, 39, 55, 66, 90+(7)	SNID (M01), M14
SN 1998fa[c]	4, −3, 18	M14
SN 2000H	−2, −1, 0, 1, 2, 3, 5, 17, 21, 32, 47, 57	SNID (B02), M14
SN 2003bg[d]	−19, −17, −15, −7, 12, 16, 20, 21, 90+(6)	H09
SN 2004ff[e]	−1	M14
SN 2006el	−4, 10, 11, 12, 13, 16, 17	M14
SN 2006T	−14, −12, 6, 7, 14, 90+(2)	S12, M14
SN 2008ax	−20, −19, −18, −16, −15, −13, −12, −11, −10, −9, −8, 6, 8, 9, 9, 12, 15, 16, 19, 23, 38, 45, 67, 74, 80, 90+(1)	M10, M14
SN 2008bo	−10, −7, −3, −1, 16, 21, 25, 31, 45, 54, 54, 90+(1)	M10, M14
SN 2009mg	−4, −1, 3, 3, 12, 13, 14, 24, 39, 39, 88	O12
SN 2011dh[f]	−17, −16, −15, −14, −13, −12, −11, −10, −9, −4, −1, 3, 4, 5, 6, 7, 9, 10, 11, 13, 15 19, 23, 27, 28, 31, 37, 46, 50, 61, 68	A11, E14, Ma14
SN 2011ei	−14, −10, −6, −4, −3, 3, 8, 13, 17, 38, 48, 66, 90+(3)	M13
SN 2011fu	−14, −13, −11, 2, 17, 19, 42, 71	K13

[a] Phases are in the rest-frame with respect to maximum light and rounded to the nearest whole day. The number in a bracket is the number of spectra with phases larger than 90 days after the date of maximum light, which we include for completeness, but do not analyze here. All dates are indicated with respect to maximum light in the (rest frame) V-band, either directly measured, or transformed (see below). The references for the date of V-band maximum light are the same as references in the third column or otherwise noted.

[b] References: SNID = in SNID release version 5.0 via templates-2.0 by Blondin & Tonry (2007), with the original references in parentheses; J94 = Jeffery et al. (1994); B95 = Barbon et al. (1995); M00 = Matheson et al. (2000b); F05 = Fransson et al. (2005); M01 = Matheson et al. (2001); M14 = Modjaz et al. (2014); B02 = Branch et al. (2002); H09 = Hamuy et al. (2009); S12 = Silverman et al. (2012b); M10 = Milisavljevic et al. (2010); O12 = Oates et al. (2012); A11 = Arcavi et al. (2011); E14 = Ergon et al. (2014); Ma14 = Marion et al. (2014); M13 = Milisavljevic et al. (2013); K13 = Kumar et al. (2013).

[c] For this SN, we converted the date of maximum light in the R-band to the date in the V-band using the relationship found by Bianco et al. (2014).

[d] Hamuy et al. (2009) regarded this SN as a broad-line SN IIb because its early spectra are broad and its inferred kinetic energy of explosion is large (Mazzali et al. 2009).

[e] For this SN, the date of V-band maximum light is 2453313.69 ± 0.90, which was determined from the V-band photometry in Drout et al. (2011) through the polynomial fitting in Bianco et al. (2014).

[f] The reference for the date of V-band maximum light for this SN is Tsvetkov et al. (2012).

webpage.[8]

3.1. *Constructing Mean Spectra from SN Spectra*

Mean spectra, together with the standard deviations from the mean spectra, can characterize the spectral diversity of each SN subtype, thus they can be used to determine if a newly discovered SN belongs to a normal type or a novel type (e.g., Ib-Ca; Kasliwal et al. 2012). Since our spectra are in relative flux and we care more about SN features than SN continua, here we construct mean spectra, as well as their standard deviations, using the flattened version of our spectral sample (i.e., the corresponding SNID templates) and following the same procedure outlined in Blondin & Tonry (2007). Here, we apply the procedure to SNe IIb, SNe Ib and SNe Ic; in Modjaz et al. (2015), we also apply it to SNe Ic-bl. Our mean spectra are constructed every five days from $t_{\rm Vmax} = -20$ to $t_{\rm Vmax} = 70$ days. Here, we only show them at several specific phases (e.g., −10, 0, 10, and 20 days). Each phase includes no more than one spectrum per input SN that is within ±2 days of the corresponding phase.[9] Compared with multiple spectra per SN, one spectrum per SN in a mean spectrum will avoid bias from a SN if it contributes several spectra to the mean spectrum. If two or more spectra from the same SN are available within ±2 days of the target phase, we choose the one that is nearest to the target phase. If there is still more than one spectrum satisfying the above condition, we use the one that covers the largest optical wavelength range, or the one with the highest signal-to-noise (S/N) ratio.

In a future paper, we will construct mean spectra that contain the continua, which can be used in photometric classification (e.g., Poznanski et al. 2002) to generate model magnitudes that represent the expected photometry of different classes of SNe at a range of redshifts and with various filters. Thus, a SN can be classified by comparing the observed photometry to the expected photometry of different types of SNe at the same redshift and with the same filter.

3.2. *Absorption Velocity and Strength Measurements*

SN spectra are characterized by the presence or absence of specific lines. In order to quantify the properties of various subtypes of SNe, we shall measure the

[8] http://cosmo.nyu.edu/SNYU/

[9] This phase range is for the phases rounded to the closest integer, which is the same as the phase range of ±2.5 days (i.e., five-day bins) for the phases rounded to tenths. Hereafter, we use ±2 days for convenience.

Table 2
Spectral sample of SNe Ib

SN Name	Phases[a] of Spectra	References[b]
SN 1983N	4, 12, 90+(1)	SNID (Wheeler)
SN 1984L	8, 9, 12, 13, 28, 32, 37, 38, 39, 57, 70, 71	SNID (Wheeler)
SN 1990I	11, 19, 40, 41, 51, 65, 88, 90+(1)	SNID (E04)
SN 1990U	11, 12, 34, 41, 70, 90+(1)	SNID (M01)
SN 1998dt[c]	2, 3, 6, 9, 10, 13, 14, 19, 34	SNID (M01), M14
SN 1999dn	−7, −1, 0, 3, 6, 12, 13, 17, 20, 41, 67	SNID (M01), B11
SN 1999ex[d]	−5, 0, 9	SNID (H02)
SN 2004dk[e]	14, 17, 46	M14
SN 2004gq[c]	−9, −8, −7, −6, −5, −2, −1, 0, 16, 17, 18, 21, 21, 25, 42, 55, 70, 73, 78, 84, 89, 90+(3)	M14
SN 2004gv	13, 15, 19, 48	M14
SN 2005bf[f]	−20−(7), −9, −7, −6, −5, −4, −3, −2, −1, 0, 1, 2, 2, 4, 5, 7, 22, 22, 24, 25, 28, 29, 32	SNID (T05, F06), M14
SN 2005hg	−14, −13, −11, −10, −9, −8, −7, −6, −5, −4, −3, −2, −1, 12, 16, 22, 26, 87	M14
SN 2006ep	−8, 8, 10, 12, 44	M14
SN 2007ag	−1, 3, 9	S12, M14
SN 2007C	−6, −5, −1, −1, 1, 7, 12, 14, 27, 37, 42, 55, 61, 63, 64, 71	S12, M14
SN 2007kj	−1, 4	M14
SN 2007Y	−15, −9, −2, 5, 8, 13, 20, 38, 90+(4)	SNID (S09)
SN 2008D[g]	−19, −18, −16, −16, −15, −14, −13, −11, −9, −8, −4, −4, 2, 3, 4, 5, 9, 11, 13, 14, 18, 19, 27, 30, 33, 41, 49, 63	M09, Mo09, M10, M14
SN 2009iz	−14, −10, 5, 11, 12, 13, 21, 42, 47	M14
SN 2009jf	−18, −17, −16, −15, −13, −11, −10, −10, −9, −7, −5 to −1, 0, 1, 1, 3, 3, 7, 9, 11, 18, 24, 25, 27, 30, 31, 33, 34, 47, 49, 55, 59, 61, 67, 70, 80, 81, 82, 90+(7)	S11, V11, M14
iPTF13bvn[h]	−16, −15, −14, −13, −12, −11, −9, −7, −6, −6, −2, −1, 1, 8, 20, 34	C13, F14

[a] Phases are in rest-frame and rounded to the nearest whole day. The number in a bracket is the number of spectra with phases larger than 90 days after or smaller than 20 days before the date of maximum light. All dates of maximum light were measured in the V-band. The references for the date of V-band max are the same as references in the third column unless otherwise noted.
[b] References: SNID = in SNID release version 5.0 via templates-2.0 by Blondin & Tonry (2007), with the original references in parentheses; Wheeler = University of Texas spectral library, which is no longer in use; E04 = Elmhamdi et al. (2004); M01 = Matheson et al. (2001); M14 = Modjaz et al. (2014); B11 = Benetti et al. (2011); H02 = Hamuy et al. (2002); T05 = Tominaga et al. (2005); F06 = Folatelli et al. (2006); S12 = Silverman et al. (2012b); S09 = Stritzinger et al. (2009); M09=Malesani et al. (2009); Mo09 = Modjaz et al. (2009); M10=Moskvitin et al. (2010); S11 = Sahu et al. (2011); V11 = Valenti et al. (2011); C13 = Cao et al. (2013); F14 = Fremling et al. (2014).
[c] For this SN, we converted the date of maximum light in the R-band to the date in the V-band using the relationship found in Bianco et al. (2014).
[d] For this SN, the initial classification was an SN Ib/c event by Hamuy et al. (2002), whereas Parrent et al. (2007) support the Ib classification and SNID also regards it as a Ib SN. Thus, we classify it as a SN Ib in this study.
[e] For this SN, the date of V-band maximum light is 2453241.18 ± 0.98, which was determined from the V-band photometry in Drout et al. (2011) through the polynomial fitting in Bianco et al. (2014).
[f] The V-band light curve of this SN shows two distinct maxima. In this study, the phases are expressed in days from the date of the second maximum light according to Modjaz et al. (2014).
[g] This SN had spectra that resemble SN Ic-bl spectra after explosion, i.e., 15 to 10 days before the date of maximum light, but developed narrow-line spectra with helium by the date of maximum light (Mazzali et al. 2008; Modjaz et al. 2009; Mazzali et al. 2009).
[h] For this SN, the date of V-band maximum light is 2456476.27 ± 0.02, which was determined from the V-band photometry in Fremling et al. (2014) through the polynomial fitting in Bianco et al. (2014).

velocity and strength of specific absorption lines in each spectrum. We did so by following the same procedure used for SN Ia spectra in Blondin et al. (2006), Blondin et al. (2011, see their figure 15), and Silverman et al. (2012a, see their figure 2), as outlined below.

We used the following steps to measure the velocity of absorption features in spectra. First, a quadratic polynomial was fitted around the minimum of the concerned absorption feature to find the exact wavelength position that corresponds to the minimum flux. Second, the relativistic Doppler formula was applied to the wavelength found above. We used the equivalent width (EW) to quantify the strength of the absorption features. First, a median filter was applied to both sides of the absorption feature to find the local maxima. A straight line connecting one local maximum on the blue side and one local maximum on the red side was regarded as the local continuum or pseudo continuum.[10] If there were more than one local maximum on either or both sides, the pair of local maxima that ensures the pseudo continuum slope does not cross the spectrum within the boundaries of the feature was picked. If no pair of local maxima satisfied this condition, the pair with the highest local maxima was picked. If more than one pair of local maxima satisfied this condition, the pair that maximized the wavelength range was picked. The resultant

[10] "Local" or "pseudo" is due to the fact that there is no one source for the continuum.

pseudo continuum was used to calculate the EW, which will be called "pseudo EW" (pEW; Blondin et al. 2011; Silverman et al. 2012a). The pEW has the following definition,

$$\mathrm{pEW} = \sum_{i=0}^{N_d-1} \Delta\lambda_i \left(\frac{f_c(\lambda_i) - f(\lambda_i)}{f_c(\lambda_i)} \right), \quad (1)$$

where N_d is the number of data points between two local maxima, λ_i is the wavelength of the ith data point, $\Delta\lambda_i$ is the bin size between λ_i and λ_{i+1}, $f_c(\lambda_i)$ is the flux of local continuum at λ_i, and $f(\lambda_i)$ is the flux at λ_i. One advantage of using the pEW to quantify the strength of absorption lines is that no assumption about the line profile is made.

We adopt the line identifications for stripped SNe of Branch et al. (2002, 2006), Elmhamdi et al. (2006), and Dessart et al. (2012), as well as other works in the literature included in this study that identified lines in the spectra of a specific stripped SN (see Sections 4 and 5). Since stripped envelope SNe have been observed to start transitioning from the photospheric phase to the nebular phase at generally 60 days after the date of maximum light (e.g., Barbon et al. 1990; Filippenko et al. 1995; Iwamoto et al. 2000; Matheson et al. 2001), in this work, we only show our measurements at phases before $t_{\mathrm{Vmax}} \simeq 60$ days. We note that our line identifications are not definitive; furthermore, we discuss below some of the features for which contradictory identifications exist in the literature. We also assume that the pEW of an absorption feature can reflect the amount of atoms of the corresponding element at the corresponding state in the ejecta.

3.3. *Error Bars of the Measurements*

We used the uncertainty arrays derived in Appendix B and a Monte Carlo (MC) sampling method to estimate errors of the above measurements. Assuming the noise at a wavelength bin in a spectrum obeys a Gaussian distribution and equals one standard deviation of the distribution, a synthetic spectrum was generated by drawing a data point for each wavelength bin within a Gaussian distribution centered on the original spectral datum, and with a standard deviation equal to the value for the same wavelength bin in the uncertainty array of the original spectrum. For each synthetic spectrum, we repeated the steps in the velocity and pEW measurements in Section 3.2. The estimated measurement and error bar were calculated as the mean and standard deviation of the corresponding values across 3000 realizations. The number of realizations should be larger than $N_d(\log N_d)^2$ (Babu & Singh 1983), where N_d is the number of data points in the portion of the resampled spectrum. The 3000 realizations are sufficient in our case since we only have a few tens of data points for each SN feature.

For the velocity and pEW measurements, the typical MC uncertainties are $\sim \pm 1000$ km s^{-1} and $\sim \pm 10$ Å, respectively. The sources of error include the spectral quality (i.e., S/N ratio) and line blending that gives rise to broad features.

A subset of our measurements is shown in Tables 3 and 4. A full version of this table is available in a machine-readable form in the online journal.

4. IS THERE A CONTINUUM BETWEEN PROGENITORS OF SNE IIB AND SNE IB?

Our ultimate goal is to map different progenitor models to different SN subtypes. Thus, it is important to correctly classify SNe as the first step. In general, SNe are classified based on spectra and light curves. It is not always easy to classify SNe because SN spectra are time dependent and even the spectra at the same phase are diverse within a SN subtype. The time-dependent nature of spectra is claimed to affect most classifications of SNe IIb and Ib (e.g., Milisavljevic et al. 2013). That is because by definition, SNe IIb are similar to SNe II at early phases, but over time they evolve to appear more analogous to SNe Ib. Thus, there are concerns that a SN IIb may be misclassified as a SN Ib if it is not discovered early enough (e.g., Milisavljevic et al. 2013). In this section, we show that this concern is not well-founded by investigating the presence of Hα in SNe Ib (Section 4.1), exploring the behavior of important common lines in SNe IIb and Ib, and concluding that we can use the pEW of Hα (Section 4.2) to distinguish between these two SN subtypes. Moreover, there are observational continua between the spectral properties of SNe IIb and those of SNe Ib, based on measurements of Hα, He I lines, and Fe II λ5169 (Sections 4.3–4.5, respectively). We also explore the possibility of the existence of subtypes within SNe Ib (Section 4.6).

4.1. *Is There Hα in the Spectra of SNe Ib?*

While the absence of Hα is supposed to be the hallmark of SNe Ib, there are good reasons to assume that there may be some Hα in SNe Ib (e.g., Deng et al. 2000; Branch et al. 2002; Elmhamdi et al. 2006; Parrent et al. 2007; James & Baron 2010; Yoon et al. 2010; Parrent et al. 2015). Since the progenitor stars may have different amounts of hydrogen present before explosion (since the various mechanisms may not have removed all of the hydrogen), we may expect different amounts, including small amounts, of hydrogen still present at the time of explosion. However, it is not easy to identify Hα because the absorption feature at the expected position of Hα—the "6300 Å absorption line"—can be due to C II λ6580, Ne I λ6402 or Si II λ6355 as well (e.g., Branch et al. 2002; Tominaga et al. 2005; Elmhamdi et al. 2006; Parrent et al. 2007).

Previous investigations include modeling progenitors of SNe Ib to investigate whether there is a hydrogen layer before explosion, as well as comparing the synthetic spectrum from radiative transfer calculations to the observed spectrum. Applying stellar evolutionary models that include the effects of rotation to binary systems, Yoon et al. (2010) found that the progenitor of SNe Ib should have a thin hydrogen layer before explosion. Thus, it is likely that the spectra of SNe Ib show Hα in absorption. Moreover, many works (e.g., Deng et al. 2000; Branch et al. 2002; Elmhamdi et al. 2006; Parrent et al. 2007; James & Baron 2010; Parrent et al. 2015) identified Hα in the spectra of SNe Ib using various spectral synthesis codes such as SYNOW (a parameterized SN spectrum-synthesis code; Parrent et al. 2010), PHOENIX (a generalized non-local thermodynamic equilibrium stellar atmospheres code; Hauschildt & Baron 1999, 2004), or non-local thermodynamics equi-

Table 3
Measured absorption velocities

Phase[a] (days)	He I λ5876[b] (km s^{-1})	He I λ6678[b] (km s^{-1})	He I λ7065[b] (km s^{-1})	Hα[b] (km s^{-1})	Fe II λ5169[b] (km s^{-1})	O I λ7774[b] (km s^{-1})
			SN 1983N			
4	−9600 ± 600	−8900 ± 600	···	−14300 ± 500	−8900 ± 1500	···
12	−10200 ± 700	−9900 ± 700	−7500 ± 300	−12500 ± 500	−6200 ± 700	···

Note. — This table is available in its entirety in a machine-readable form in the online journal. A portion is shown here for guidance regarding its form and content.
[a] Rest-frame age of spectrum in days relative to V-band maximum. See text for details.
[b] For multiple velocity measurements for the same SN of different spectra taken on the same night, the weighted average is reported, and the velocity error reported here is the standard deviation of the weighted average.

Table 4
Measured pEW values

Phase[a] (days)	He I λ5876 (Å)	He I λ6678 (Å)	He I λ7065 (Å)	Hα (Å)	O I λ7774 (Å)
		SN 1983N			
4	114 ± 4	31 ± 3	···	28 ± 3	···
12	122 ± 4	43 ± 4	105 ± 8	30 ± 10	···

Note. — This table is the same as Tabel 3, but for pEW values.

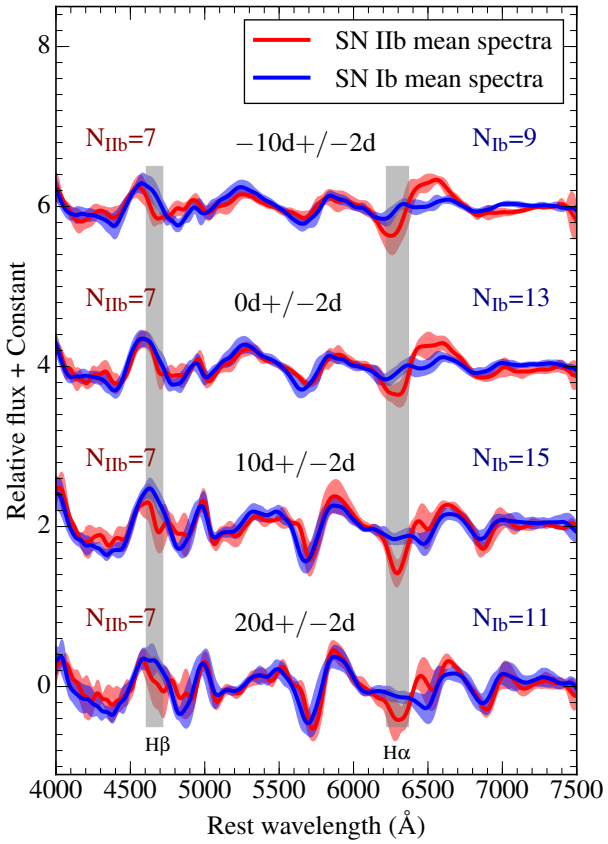

Figure 1. Mean spectra and their corresponding standard deviations of SNe IIb (red) and SNe Ib (blue) at four different phase ranges: $t_{\rm Vmax}$ = −12 to −8, −2 to 2, 8 to 12, and 18 to 22 days. Each mean spectrum only includes one spectrum per SN even if multiple spectra have been taken within the phase range. $N_{\rm IIb}$ represents the number of spectra (which is also the number of SNe) included in the mean spectrum of SNe IIb at each phase, and $N_{\rm Ib}$ represents the number of spectra for SNe Ib. The gray vertical bands indicate the expected positions of Hα and Hβ at velocities of −9000 km s^{-1} to −16000 km s^{-1}.

librium time-dependent radiative-transfer calculations (Dessart et al. 2012).

Here, we use a statistical and data-driven approach to investigate whether there is Hα present in SN Ib spectra. We use the fact that SNe IIb, by definition, show unambiguous lines of Hα in their spectra and compare the mean spectra of SNe IIb with those of SNe Ib. First, we identified Hα and Hβ in the mean spectra of SNe IIb. Then, we searched for Hα and Hβ at similar velocities (i.e., blueshift) in the mean spectra of SNe Ib. In Figure 1, we present the mean spectra of SNe IIb and SNe Ib, which were constructed using the flattened version of our SN sample, at several specific phase ranges: $t_{\rm Vmax} = -10\pm2$, 0 ± 2, 10 ± 2, and 20 ± 2 days. The mean spectra of SNe IIb show a strong Hα P-Cygni profile at $t_{\rm Vmax} = -10$ and 0 days, a pronounced Hα absorption feature (assuming the absorption feature around 6300Å is due to Hα) at $t_{\rm Vmax} = 10$ and 20 days, and a weak Hβ absorption feature (assuming the absorption feature around 4700Å is due to Hβ) at all phases. In the mean spectra of SNe Ib, there are absorption features at the expected positions of Hα at $t_{\rm Vmax} = -10$, 0, and 10 days. Thus, it is reasonable to identify these absorption features as Hα. At $t_{\rm Vmax} \simeq -10$ days and $t_{\rm Vmax} \simeq 0$ day, the Hα absorption features in the SN Ib mean spectra are weaker and at a higher velocity than those in the SN IIb mean spectra. At $t_{\rm Vmax} \simeq 10$ days, the Hα absorption feature in the SN Ib mean spectrum is much weaker than that in the SN IIb mean spectrum but the Hα absorption features are at a similar velocity in both mean spectra. After $t_{\rm Vmax} \simeq 20$ days, it is very hard to detect the Hα absorption feature in the spectra of SNe Ib.

While we cannot conclusively verify the detection of Hα in all SNe Ib, in the following sections we assume that the weak absorption feature at $\sim$ 6250 Å around the date of maximum light in SN Ib spectra is due to Hα and report its pEW values and absorption velocities. We caution that the same absorption feature may be due

to different elements at different phases.[11]

4.2. *The Hα Line Behaves Differently in SNe IIb and SNe Ib*

As shown in Section 4.1, we assume that some Hα is present in SNe Ib in our sample, and thus we can use it as a diagnostic to compare SNe IIb with SNe Ib. The Hα line in the spectra of SNe IIb becomes weaker and even disappears with time. Hence, there are concerns that a SN IIb may be misclassified as a SN Ib if it is not discovered early enough (e.g., Dessart et al. 2011; Milisavljevic et al. 2013). In this section, we show that these concerns may not apply since the pEW values of Hα evolve differently in SNe IIb compared to those in SNe Ib. Thus, the observed spectra of SNe IIb are different from those of SNe Ib, even at later phases, indicating that SNe IIb are distinguishable from SNe Ib.

Assuming the absorption feature around 6300Å is due to Hα, the temporal evolution of the Hα velocity and pEW values of individual SNe IIb and Ib, as well as the rolling weighted averages (see Appendix D) for the two SN subtypes, are displayed in Figure 2.[12] In particular, the weighted averages at $t_{\rm Vmax} \simeq 0$ day are listed in Table 6. As mentioned before, five and seven SNe in our sample, respectively, were also included in Branch et al. (2002) and Elmhamdi et al. (2006). Both papers used SYNOW to determine Hα velocities; these are consistent with Hα velocities via line identifications in this work. We observe that the average Hα velocities in SNe Ib are systematically higher (around 40% at $t_{\rm Vmax} \simeq 0$ day) than in SNe IIb. If SNe IIb and Ib have almost the same explosion energies, then SNe Ib have a thinner hydrogen envelope or a lower hydrogen mass than SNe IIb. The Hα velocities of individual SNe Ib show that they drop rapidly over phase intervals during which they are detected. However, the rolling weighted average velocities stay approximately the same after $t_{\rm Vmax} \simeq 10$ days due to one SN Ib (SN 2004gv) with high Hα velocities starting at $t_{\rm Vmax} \simeq 15$ days and ending at $t_{\rm Vmax} \simeq 20$ days. The Hα velocities in SNe IIb decrease rapidly from $t_{\rm Vmax} \simeq -10$ days to $t_{\rm Vmax} \simeq 0$ day and have a relatively flat evolution after that. There is much overlap between the SN IIb and SN Ib velocities around $t_{\rm Vmax} = 15$ days.

The average Hα pEW values in SNe IIb are systematically higher (~ 4 times at $t_{\rm Vmax} \simeq 0$ day) than in SNe Ib. This confirms that, compared to SNe Ib, SNe IIb have more hydrogen in their progenitors. There is a larger scatter in the pEW values of SNe IIb than in SNe Ib. The pEW values of Hα form two distinct groups for SNe IIb and SNe Ib, except for three SNe Ib (SNe 1999dn, 1999ex, and iPTF13bvn) on the lower bound of the SN IIb sample. Since there is almost no overlap between SNe IIb and SNe Ib, the Hα pEW can be used to differentiate SNe IIb from SNe Ib at all epochs. The concern of Milisavljevic et al. (2013) that if a SN IIb is discovered several days after the date of maximum light, the SN IIb may be misclassified as a Ib, is not well-founded since even at later phases, a SN IIb will always have a larger Hα pEW than a SN Ib.

Milisavljevic et al. (2013) suggested using the ratios of He I λ5876 pEW values to Hα pEW values to differentiate SNe IIb from SNe Ib. We found that this criterion is driven by the pEW values of Hα, since as shown in Section 4.4, the pEW values of He I λ5876 in SNe IIb and SNe Ib are similar. Thus, we suggest to use the pEW values of Hα to classify SNe IIb and Ib. In particular, we plot SN 2011ei, the SN in Milisavljevic et al. (2013), in Figure 2, which indeed shows that even if SN 2011ei was discovered after $t_{\rm Vmax} \simeq 10$ days, it would not have been classified as a SN Ib.[13] To mimic the situation where SN 2011ei was discovered one week after $t_{\rm Vmax} \simeq 0$ day or later, we ran SNID on its spectra at $t_{\rm Vmax} = 8$, 13, and 17 days. The SNID code identifies these spectra as SN IIb spectra as well. In particular, using the default definition of matched SN spectra in SNID, the ratio between the number of matched SNe IIb and that of SNe Ib ranges from 1.3 to 2.3.

4.3. *Absorption Velocities of He I Lines in SNe IIb and SNe Ib*

In the optical spectra of SNe IIb and Ib, the three strongest He I lines are He I λλλ5876, 6678, and 7065. In the following, we will first present the temporal evolution of the velocities of these He I lines. Then we will explore the so called "flat-velocity" SNe IIb (Folatelli et al. 2014) in our sample as well.

Figure 3 presents the temporal velocity evolution of He I λλλ5876, 6678, and 7065 for SNe IIb and Ib, respectively. The left panels show the velocity evolutions of individual SNe IIb and Ib, while the right panels show the corresponding rolling weighted averages for the two SN subtypes. In particular, the weighted averages at $t_{\rm Vmax} \simeq 0$ day are listed in Table 6. As mentioned before, five and seven SNe in our above sample were in Branch et al. (2002) and Elmhamdi et al. (2006), respectively. Both papers determined He I velocities using SYNOW. For the SNe we have in common, their He I λλλ5876, 6678, 7065 velocities via line identifications in this work are consistent with the values reported by Branch et al. (2002) and Elmhamdi et al. (2006).

There is a wide overlap in the He I velocities for SNe IIb and SNe Ib, indicating a continuum of some physical parameters such as the positions of the helium layer in the progenitors, the conditions for non-thermal excitation, or both. The average velocities of He I λλλ5876, 6678, 7065 in SNe Ib are slightly higher than those in SNe IIb. Assuming SNe IIb and Ib have similar explosion energies, SNe Ib may have lost some of the helium layer, which results in a smaller ejecta mass and a higher velocity in the remaining helium layer.

In general, the He I velocities evolve to lower values over time, with the He I λλ5876, 6678 velocities in SNe IIb and Ib decreasing more rapidly than the He I λ7065 velocities by a factor of 70% to 100% at $t_{\rm Vmax} \simeq 0$ day. However, as shown in Figure 4, the He I velocities in

[11] For example, as claimed in Tominaga et al. (2005), the line near 6300 Å in spectra of SN 2005bf is reproduced as a blend of Hα and Si II λ6355 at the time of the first peak, while it is reproduced as Si II λ6355 alone at the time of the second peak.

[12] Due to the difficulty of detecting Hα in the spectra of SNe Ib at phases later than $t_{\rm Vmax} \simeq 25$ days, no data points of SNe Ib are shown at these phases.

[13] Milisavljevic et al. (2013) identified a two-component Hα absorption in SN 2011ei. For SN 2011ei and other SNe that have two-component Hα absorptions, we measure absorption velocity using the dominant component and pEW using both components.

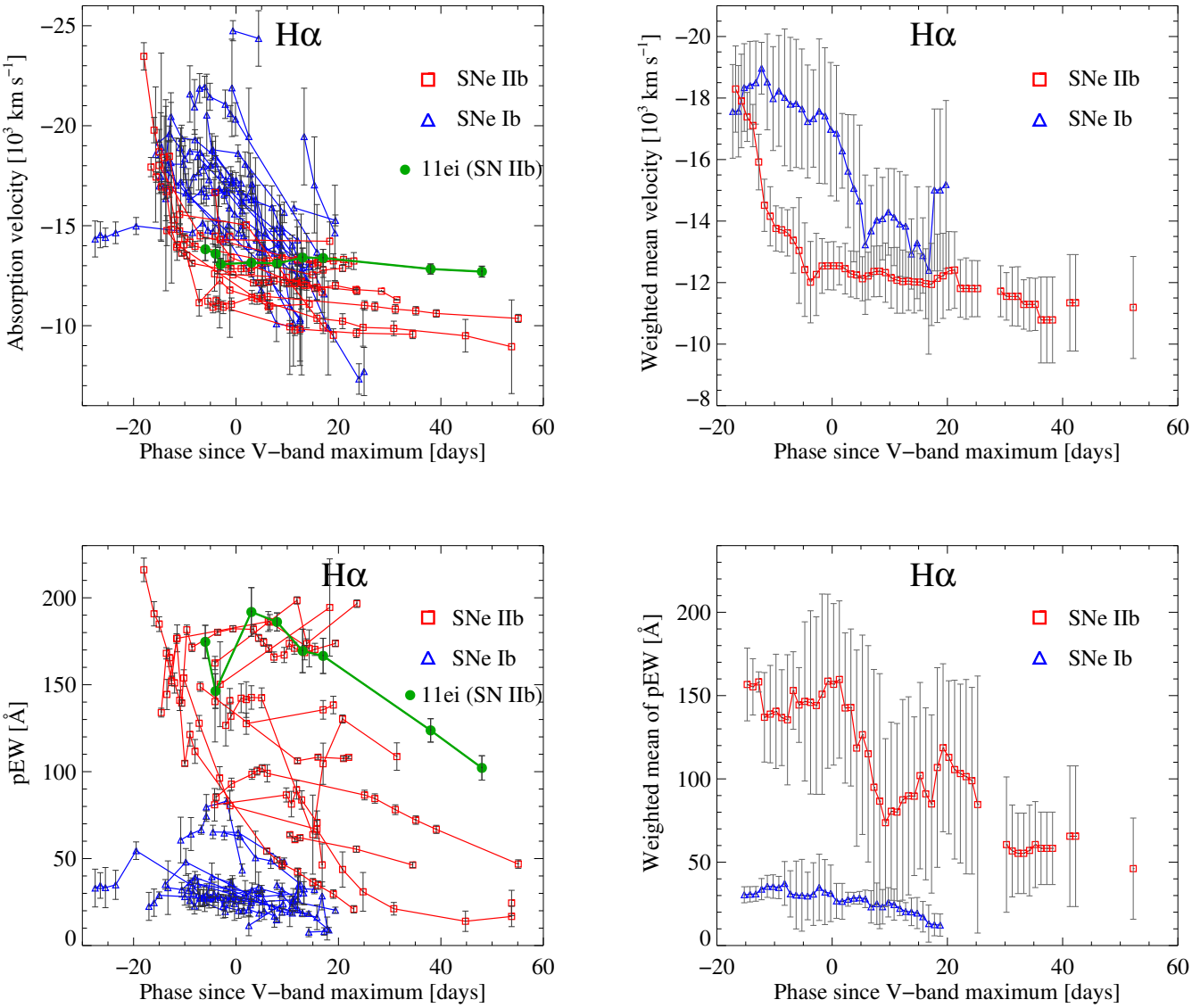

Figure 2. Measured Hα velocities (*Top*) and pEW values (*Bottom*) for SNe IIb (red squares) and SNe Ib (blue triangles). *Left*: velocities and pEW values for individual SNe. Data of the same SN are connected by a line. The SN Ib that has data earlier than $t_{\rm Vmax} = -20$ days is SN 2005bf. The evolution of SN 2011ei is also shown (see text for more discussion). In the lower left panel, the three SNe Ib and one SN IIb that have nearly overlapping values are SNe 1999dn, 1999ex, iPTF13bvn, and 2008ax. *Right*: Rolling weighted average values for SNe IIb and SNe Ib, with a bin size of five days for phases before $t_{\rm Vmax} = 30$ days and a bin size of 10 days for phases thereafter. In order to show the distribution of the data, the error bars on the mean values represent the standard deviation of the contributing data points. For the standard deviation to be meaningful, only weighted average values constructed from more than three SNe are shown. There are no data for SNe Ib at $t_{\rm Vmax} > 25$ days because it is very difficult to identify Hα in the spectra of SNe Ib at those phases. Note that there is almost no overlap between pEW values of Hα in SNe IIb and SNe Ib, thus the Hα pEW defines SNe IIb and Ib, i.e., the Hα pEW values can be used to differentiate SNe IIb from SNe Ib at all epochs.

SNe 2005bf and 2011dh increase with time, if the He I λ5876 velocities at the earliest phase are ignored. As explained in Tominaga et al. (2005), the increasing He I velocities may be the result of increasing non-thermal excitation.

Folatelli et al. (2014) introduced a family of flat-velocity SNe IIb (SNe fvIIb) whose velocities stay roughly the same—between 6000 and 8000 km s^{-1}—during the photospheric phase. They argue that this may indicate a dense shell in the ejecta, though its formation lacks a physical mechanism. In particular, Folatelli et al. (2014) showed the evolution of the He I λ5876 velocity in their SN sample and claimed five SNe fvIIb: SNe 1999ex, 2005bf, 2007Y, 2010as, and 2011dh. We agree that the velocities of He I lines for these SNe evolve slowly compared to other SNe. However, we argue that the first three SNe are flat-velocity SNe Ib (SNe fvIb), based on classifications in other literature and measurements in this work, as summarized in Table 5. Except for SN 2010as, which is not included in our sample (since we only include SN spectra available before September of 2014 and spectra of SN 2010as were not accessible before that date), we confirm that the remaining four flat-velocity SNe have relatively flat velocities

Table 5
Classifications of three flat-velocity SNe

SN name	Classification in Folatelli et al. (2014)	Classification in some works and this work
SN 1999ex	IIb	Ib (Parrent et al. 2007) [a]
SN 2005bf	IIb	Ib (Modjaz et al. 2014) [b]
SN 2007Y	IIb	Ib (Stritzinger et al. 2009) [c]

[a] Although the Hα pEW value in SN 1999ex is within the nearly overlapping region for SN IIb and SN Ib samples, the Hα velocity and behavior of He I lines in its spectra are consistent with SNe Ib in our sample.
[b] SN 2005bf does not have strong H-alpha line (as shown in the bottom panel of Figure 2), which by definition is the case for SNe Ib instead of SNe IIb.
[c] Although the time evolution of He I λ7065 pEW values in SN 2000Y is comparable to that of SNe IIb, the pEW values and velocities of Hα and other He I lines in this SN are more consistent with those of SNe Ib in our sample.

of He I $\lambda\lambda$6678 and 7065 as well.

Figure 5 shows seven SNe fvIIb and fvIb in our sample that satisfy the following conditions: each SN has spectra around the date of maximum light, i.e., $-5 < t_{\rm Vmax} < 5$ days; spectra cover more than 10 days; ignoring early phases ($t_{\rm Vmax} < -10$ days), the velocities for He I $\lambda\lambda\lambda$ 5876, 6678, and 7065 stays roughly the same, i.e., the change in velocity is smaller than 2000 km s^{-1}. In addition to the SNe mentioned in Folatelli et al. (2014), we identify SNe 1998dt, 2006el and 2009mg as new flat-velocity SNe. Thus, using the He I velocities, we suggest there are four SNe fvIIb (SNe 2006el, 2009mg, 2010as, and 2011dh) and four SNe fvIb (SNe 1998dt, 1999ex, 2005bf, and 2007Y) based on our work. Since none of them show flat-velocity Fe II lines and only two of them (SNe 2006el and 2005bf) have flat-velocity Hα lines, the flat-velocity He I lines formed in these SNe could rather be due to e.g., excitation effects since the He I lines are due to non-thermal excitation (Lucy 1991), instead of a dense shell as proposed by Folatelli et al. (2014), since otherwise, other lines would have also exhibited the same flat velocities.

4.4. *Strengths of He I Lines in SNe IIb and Ib*

In this section, we first show the temporal evolution of pEW values of He I $\lambda\lambda\lambda$5876, 6678, 7065 in SNe IIb and in SNe Ib. Then, we compare the trends we found with the observations in Matheson et al. (2001).

The temporal pEW evolution of He I $\lambda\lambda\lambda$5876, 6678, and 7065 for SNe IIb and Ib are displayed in Figure 6. The pEW evolution of individual SNe IIb and Ib are shown in the left panels, and the corresponding rolling weighted averages are shown in the right panels. In particular, the weighted averages at $t_{\rm Vmax} \simeq 0$ day are listed in Table 6. There is a wide overlap in the pEW values of He I lines between SNe IIb and SNe Ib, which indicates a continuum of physical parameters, e.g., the thickness of the helium layer, in the progenitors. The He I λ5876 pEW values are indistinguishable between SNe Ib and SNe IIb at most epochs while before $t_{\rm Vmax} \simeq 0$ day, the average He I λ5876 pEW values in SNe Ib are systematically higher than those in SNe IIb although a SN IIb data point at $t_{\rm Vmax} \simeq 0$ day (SN 2004ff) is among values of our SN Ib sample. For He I λ6678 pEW values, the average values are higher in SNe Ib than in SNe IIb at most phases. The two SNe IIb that have the highest He I λ6678 pEW values are SNe 2008ax and 2011ei. The He I λ7065 pEW values behave similarly in SNe Ib and SNe IIb before $t_{\rm Vmax} \simeq 10$ days. However, SNe IIb show much stronger He I λ7065 than SNe Ib afterwards, although a SN Ib (SN 2007Y) lies in the SN IIb sample.

We did not find the same trends as those reported in Matheson et al. (2001) concerning the pEW ratios of He I lines. They claimed that for SNe Ib, He I λ5876 and λ7065 grow in strength relative to He I λ6678 over time. They chose He I λ6678 as the reference feature for two reasons. First, He I λ5876 is likely to be contaminated by Na I D and He I λ7065 is generally weaker than He I λ6678. Thus, He I λ6678 would be the cleanest and easiest one to measure in SNe IIb and Ib. Second, He I λ6678 arises from the singlet state whereas He I $\lambda\lambda$5876, 7065 arise from the triplet state. Thus, He I $\lambda\lambda$5876, 7065 should be tracked together and may be different from He I λ6678. Compared with the sample in Matheson et al. (2001), we have a larger sample and more spectra at earlier phases. Their sample is composed of three SNe Ib (SNe 1998dt, 1999di, and 1999dn), and their data begin at $t_{\rm Vmax} \simeq 10$ days; We have 21 SNe Ib (including SNe 1998dt and 1999dn), and our data begin at $t_{\rm Vmax} \simeq -10$ days. We find that for individual SNe IIb and Ib, the pEW ratios mentioned above decrease at the beginning and then stay relatively unchanged or increase slightly.

4.5. *Absorption Velocity of Fe II λ5169 in SNe IIb and Ib*

Figure 7 shows our phenomenological way to identify Fe II $\lambda\lambda\lambda$4924, 5018, and 5169, which are the main Fe II features between 4800 Å and 5100 Å. If the three lines appear blended into a "w" feature, which is more common than the lines appearing discernibly separate, the bluer absorption component is regarded as a blend of Fe II λ4924 and 5018 and the redder absorption component as Fe II λ5169. Given that Fe II $\lambda\lambda$4924 and 5018 are more difficult to identify than Fe II λ5169, here we report the velocities of Fe II λ5169 in SNe IIb and Ib, as has been done previously in the literature (e.g., Branch et al. 2002).

As shown in Figure 8, the weighted average velocities of Fe II λ5169 in SNe Ib are slightly higher than those in SNe IIb, which is consistent with the trends of He I velocities observed in SNe IIb and Ib. The two possible explanations are the same as those in Section 4.3. We also notice that the relationship between the Fe II λ5169 velocities and phase is not as tight as that claimed in Branch et al. (2002). For example, at $t_{\rm Vmax} \simeq 0$ day, the spread of Fe II λ5169 velocities in our SN Ib sample is $\sim$ 4000 km s^{-1}, while in the SN Ib sample of Branch

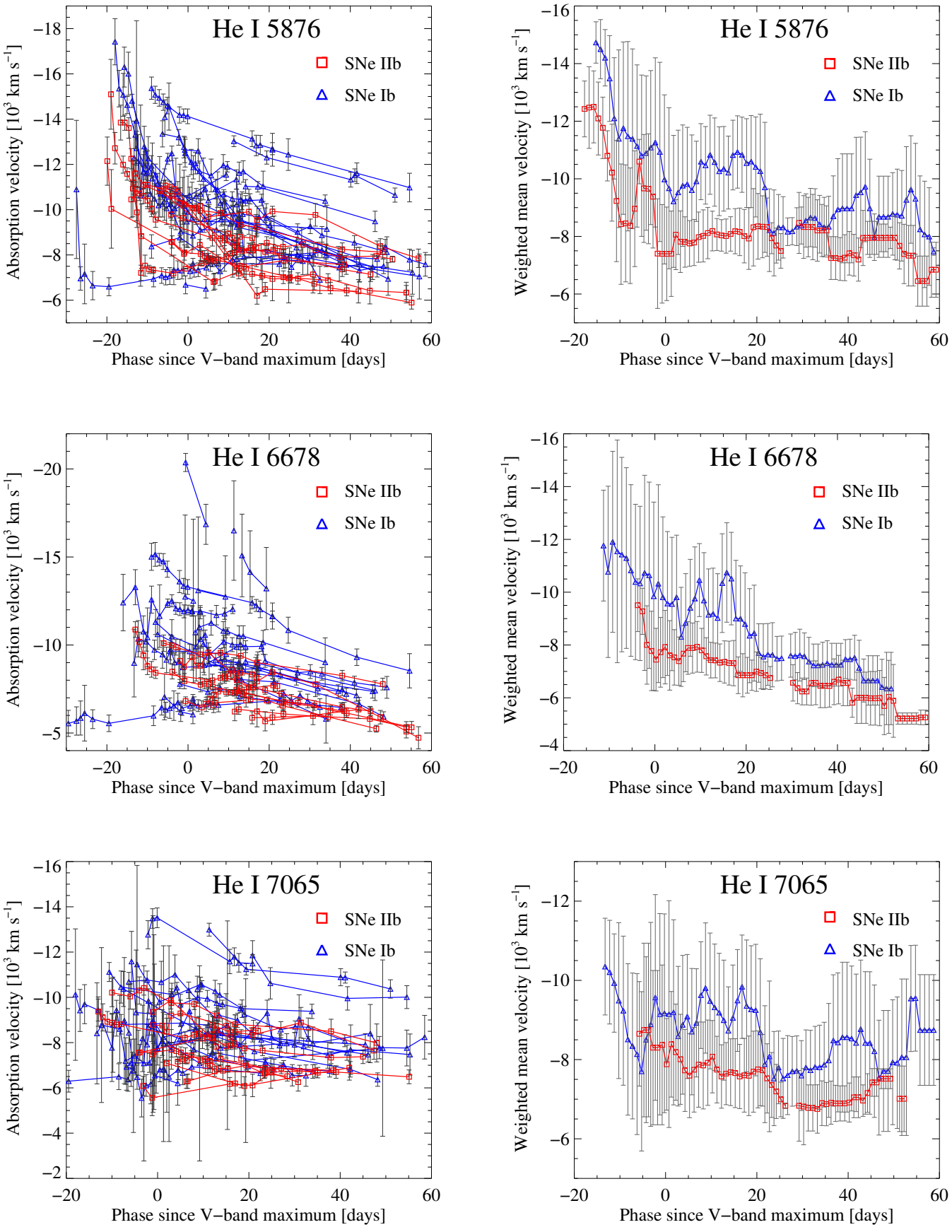

Figure 3. The same as Figure 2, but for measurements of He I λ5876 (*Top*), He I λ6678 (*Middle*), and He I λ7065 (*Bottom*) velocities. In the bottom left panel, the two SNe Ib with the highest He I λ7065 velocities are SNe 1990I and 2004gq.

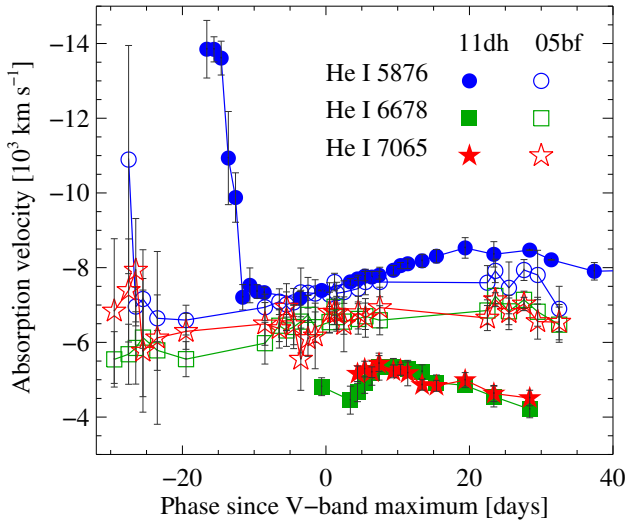

Figure 4. Measurements of He I λλλ5876, 6678, and 7065 absorption velocities for SNe 2011dh (a SN IIb) and 2005bf (a SN Ib). For clarity, the velocities for SN 2011dh are shifted downwards by 2000 km s^{-1}. We note that the velocity values do not decrease monotonically with time, which is surprising.

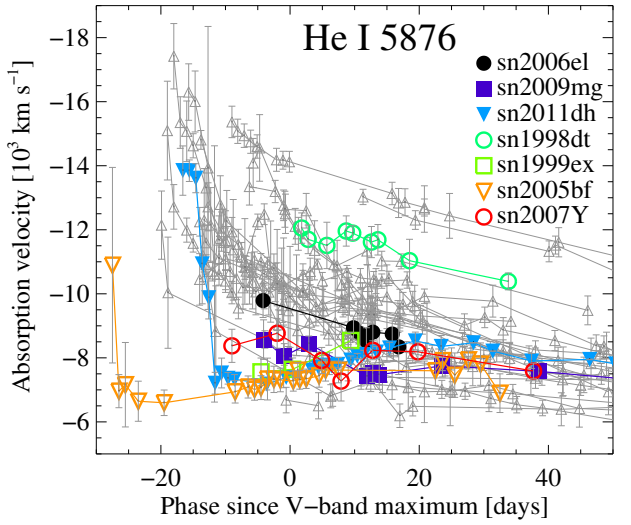

Figure 5. Measurements of He I λ5876 absorption velocities for seven flat-velocity SNe IIb and Ib in our sample. The three SNe (SNe 2006el, 2009mg, and 2011dh) with filled symbols are SNe IIb and the four SNe (SNe 1998dt, 1999ex, 2005bf, and 2007Y) with open symbols are SNe Ib. For comparison, the gray triangles are the remaining SNe IIb and Ib in our sample. Data points of the same SN are connected by a line.

et al. (2002), it is ∼ 1000 km s^{-1} (their figure 22).

Table 6 summarizes the weighted absorption velocities and pEW values for different lines in SNe IIb and Ib at $t_{\rm Vmax} \simeq 0$ day.

4.6. *Are there two classes of SNe Ib?*

Valenti et al. (2011) was the first to observe that some SNe Ib (e.g., their SN 2009jf) show weak He I λ5876 whose strength stays roughly the same after the date of maximum while others show strong He I λ5876 that increases in strength over time. We do not observe this trend using our large dataset. As shown in Figure 9, although SNe 2009jf and 2005hg seem to represent the two kinds of SNe Ib mentioned in Valenti et al. (2011), other SNe Ib significantly overlap in the He I λ5876 pEW measurements around the date of maximum light and after $t_{\rm Vmax} \simeq 50$ days. Moreover, no sign of two SN Ib subclasses is found based on the pEW values of He I λλ6678 and 7065 (see the middle left and bottom left panels of Figure 6). Thus, we do not divide SNe Ib into two classes.

5. THE HELIUM PROBLEM FOR SNE IC

While SNe Ic are defined by the apparent lack of He I lines in their spectra, there is a long-standing debate whether there is weak He or hidden He in SN Ic spectra. For the former, as discussed below in Section 5.1, some authors have claimed the detection of weak He I λ5876 or weak He I λ10830, while others disagree about these identifications. For the latter, as discussed in Section 5.2, some models suggest that helium may be present in SN Ic progenitors, but that they may not be excited via non-thermal processes due to insufficient mixing of ^{56}Ni (e.g., Dessart et al. 2012), while others argue that the SN Ic progenitors are helium-free (e.g., Hachinger et al. 2012; Frey et al. 2013; **?**). Resolving whether or not the progenitor stars of SNe Ic are truly helium-free has large implications for a number of fields, including stellar evolution of massive stars (e.g., Yoon & Langer 2005; Yoon et al. 2010; Langer 2012; Yoon et al. 2012) and the SN-GRB connection (e.g., Modjaz et al. 2015).

5.1. *Are there weak He I lines in spectra of SNe Ic?*

By definition, there are no conspicuous He I lines in the spectra of SNe Ic. However, it is instructive to attempt to detect weak He I lines in spectra of SNe Ic to see if a spectroscopic link with SNe Ib could be established. This link would be a constraint on progenitor models.

Prior works investigated the presence of He I lines in SN Ic spectra by comparing the velocity evolution (as defined from line identification) of one potential He I line to that of another potential He I line (Clocchiatti et al. 1996; Matheson et al. 2001), as well as comparing synthetic spectra—calculated via SYNOW or a Monte Carlo transport spectral synthesis code (Abbott & Lucy 1985; Mazzali & Lucy 1993; Lucy 1999; Mazzali 2000)—to observed spectra (Elmhamdi et al. 2006; Sauer et al. 2006). However, no agreement on whether there are He I lines in the spectra of SNe Ic has been reached. In particular, the identifications of He I λ5876 and He I λ10830 in SNe Ic are highly debated (Clocchiatti et al. 1996; Matheson et al. 2001; Elmhamdi et al. 2006; Sauer et al. 2006; Dessart et al. 2015)

In this work, we use a statistical approach to explore the question of whether the spectra of SNe Ic show weak He I lines, just as we explored the potential presence of weak H lines in SN Ib spectra (Section 4.1). Using the same approach, we first identified He I lines in the mean spectra of SNe Ib. Then we searched for He I lines at comparable velocities (i.e., blueshift) in the mean spectra of SNe Ic.

In Figure 10, we show the mean spectra and their corresponding standard deviations of SNe Ib and SNe Ic at various phase ranges. In the mean spectra of SNe

Table 6
Summary of weighted absorption velocity and pEW measurements for SNe IIb and Ib at $t_{\rm Vmax} \simeq 0$ day

SN type	$V_{H\alpha}$ (10^3kms^{-1})	$pEW_{H\alpha}$ (Å)	$V_{HeI5876}$ (10^3kms^{-1})	$V_{HeI6678}$ (10^3kms^{-1})	$V_{HeI7065}$ (10^3kms^{-1})	$V_{FeII5169}$ (10^3kms^{-1})	$pEW_{HeI5876}$ (Å)	$pEW_{HeI6678}$ (Å)	$pEW_{HeI7065}$ (Å)
SNe IIb	-12.5 ± 0.8	157 ± 48	-7.4 ± 1.6	-7.4 ± 1.2	-7.9 ± 1.2	-8.4 ± 1.4	41 ± 21	5 ± 4	26 ± 9
SNe Ib	-17.0 ± 2.2	31 ± 17	-10.0 ± 3.0	-9.9 ± 3.6	-8.9 ± 2.5	-9.1 ± 1.6	71 ± 15	17 ± 6	33 ± 4

Note. — The error is the standard deviation of data that contribute the weighted average value, which is consistent with the errors in the figures that show weighted average values.

Ib, He I λ5876 is visible after $t_{\rm Vmax} = -10$ and He I $\lambda\lambda$6678, 7065 become visible starting at $t_{\rm Vmax} = 0$. At the expected positions of He I λ5876, the mean spectra of SNe Ic show a broad feature but no obvious absorption feature at $t_{\rm Vmax} \simeq -10$ and 0 days, a weak absorption feature at $t_{\rm Vmax} \simeq 10$ days, and a strong absorption feature at $t_{\rm Vmax} \simeq 20$ days. However, this feature, which one might identify as He I λ5876, could be due to other elements such as Na I D, as claimed by many authors (e.g., Branch et al. 2002; Elmhamdi et al. 2006; Kumar et al. 2013; Marion et al. 2014) who use spectral synthesis calculations. Most importantly, the mean spectra of SNe Ic show no convincing signs of He I $\lambda\lambda$6678 and 7065 either. Thus, we conclude that no obvious He I lines are detected in the mean spectra of SNe Ic. Another interesting observation is that SN Ib spectra and SN Ic spectra differ at wavelengths other than the expected positions of He I lines, e.g., the Fe II feature at $\sim$ 4900 Å in SNe Ib is deeper than that in SNe Ic.

In summary, there has been no agreement on whether there are He I lines in the spectra of SNe Ic. Here, we find that there is no convincing sign of He I $\lambda\lambda$6678 and 7065 in the mean spectra of SNe Ic, and while there is a trough at the expected position of He I λ5876, it could be due to Na I D as claimed by many authors (e.g., Branch et al. 2002; Elmhamdi et al. 2006; Kumar et al. 2013; Marion et al. 2014). Thus, in this study, we will not identify He I λ5876 in our SN Ic sample. We suggest the use of non-LTE codes that properly treat non-thermal excitations to explore all our spectra for the presence of He I lines. We also suggest that for a SN Ib/c to be truly identified as a SN Ib, a very strong He I λ5876 absorption feature needs to be detected before $t_{\rm Vmax} \simeq 0$ or the three optical He I lines need to be detected in the same spectrum at $0 < t_{\rm Vmax} < 40$ days.

5.2. *Is There Helium in Progenitors of SNe Ic?*

While in the above section, we found that there is no convincing sign of weak He I lines in SN Ic spectra, it is still debated whether the absence of He I lines in optical spectra necessarily indicates the absence of helium in the ejecta. Dessart et al. (2012) argued that the progenitors of SNe Ic can have helium since it can be hidden by a low level of mixing. Frey et al. (2013), on the other hand, argued that SN Ic progenitors are helium free.

Using non-LTE radiative transfer calculations, Dessart et al. (2012) calculated the spectra produced by the explosions of two binary-star models with initial masses of 18 and 25 $M_\odot$ on the main sequence. They found that the same 18 $M_\odot$ model can reproduce spectra of SNe IIb, SNe IIc,[14] and SNe Ib, depending on the ^{56}Ni mixing level (with SNe Ib having the highest level). Similarly, they found that the same 25 $M_\odot$ model can reproduce the spectra of SNe Ic, if there is no ^{56}Ni mixing or weak mixing, and can reproduce the spectra of SNe Ib, if there is enhanced ^{56}Ni mixing. Their results indicate that SNe Ic and SNe Ib could have the same progenitors but different amounts of mixing. If that is the case, Dessart et al. (2012) predicted that SNe Ib should have redder colors, broader line profiles, and higher photospheric velocities than SNe Ic (see their figure 12).

In contrast, using a new mixing algorithm that is based on a physical analysis of 3D hydrodynamic simulations of convection, Frey et al. (2013) argued that helium is absent in the progenitors of SNe Ic because most of it is burned to oxygen. They used the TYCHO code that had been updated with this new mixing algorithm in three dimensions to calculate stellar structure of four progenitor models with zero-age main sequence masses of 15, 21, 23, and 27 $M_\odot$, respectively. They found that the stars had a hydrogen layer preceding their explosions, but much of the helium was brought into deeper and hotter layers due to enhanced mixing, and finally burned to oxygen. Assuming binary interactions can remove the hydrogen layer but not the helium layer, these stars would explode as SNe Ib/c. As shown in their figure 1, only the star with an initial mass of 15 $M_\odot$ had a normal helium shell (which is also the outermost layer) before the explosion. With the increase of initial mass, the fraction of helium in the outermost layer decreases. For the star with an initial mass of 23 $M_\odot$, the helium faction was below 15% in the outermost layer, which had a total mass of 2 $M_\odot$. In contrast, applying the classical mixing length theory to the same star resulted in 90% helium in the outermost layer that had the same total mass of 2 $M_\odot$ (Woosley et al. 2002). Using an Eulerian radiation-hydrodynamics code called RAGE (Radiation Adaptive Grid Eulerian) and the SPECTRUM code to calculate spectra and light curves, Frey et al. (2013) found that their models exhibited stronger oxygen and weaker helium lines than models based on the classical mixing length theory in Woosley et al. (2002), mainly because the helium in their models was burned into oxygen.

In order to test the predictions of Dessart et al. (2012) and Frey et al. (2013), which represent two competing models, we measured the strength and velocity of O I λ7774 and the velocity of Fe II λ5169 in SNe Ib and Ic, since each of these models predicts a different behavior

[14] As explained in Dessart et al. (2012), SNe IIc refer to SNe that show a strong Hα line initially but then show no H I, He I, or Si II in the optical after $t_{\rm Vmax} \simeq 15$ days. This SN subtype has not been observed.

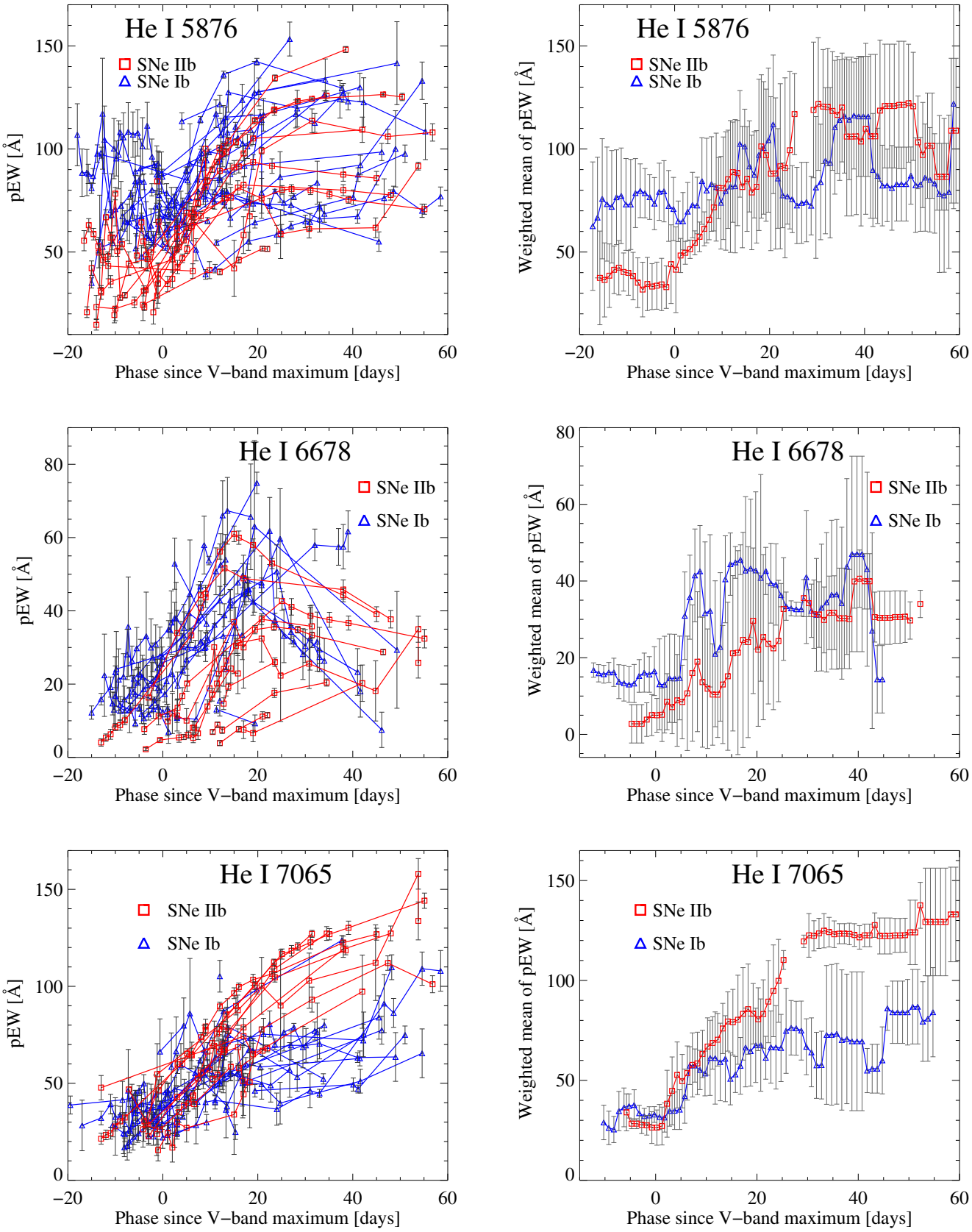

Figure 6. The same as Figure 2, but for pEW measurements of He I λ5876 (*Top*), He I λ6678 (*Middle*), and He I λ7065 (*Bottom*). In the top left panel, the SN IIb that lies in the SN Ib sample at $t_{\rm Vmax} \simeq 0$ day is SN 2004ff. In the middle left panel, the two SNe IIb with the strongest He I λ6678 pEW values are SNe 2008ax and 2011ei. In the bottom left panel, the SN Ib that lies in the SN IIb sample after $t_{\rm Vmax} \simeq 20$ days is SN 2007Y.

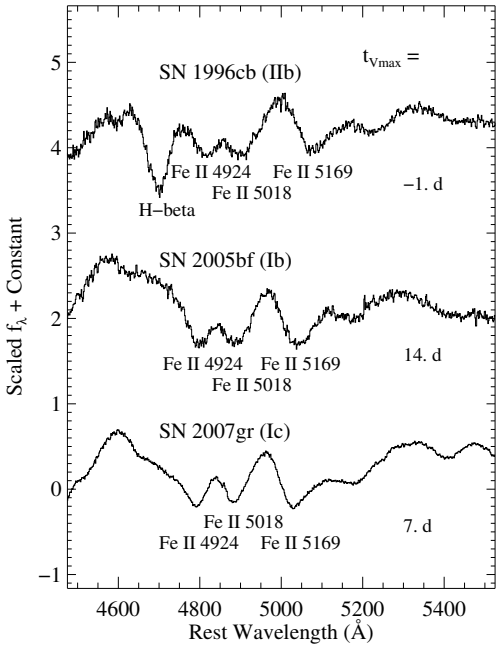

Figure 7. The Fe II triplet region for spectra of three different SNe at various phases.

of one or all observables.

5.2.1. *Strength of O I λ7774*

As discussed above, Dessart et al. (2012) argued that if the progenitors of SNe Ib and SNe Ic have the same composition, but different ^{56}Ni mixing levels (i.e., they both have the helium layer but SNe Ib have a higher ^{56}Ni mixing level than SNe Ic), then SNe Ib will have stronger lines than SNe Ic. Frey et al. (2013) found that their models—which have adapted a new mixing algorithm—show stronger oxygen and weaker helium lines than models based on the classical mixing length theory in Woosley et al. (2002). In this section, we choose to measure the strength of the O I λ7774 line to test predictions made by both papers.[15]

Another reason to measure the strength of O I λ7774 is to compare it with the observation of Matheson et al. (2001) that the line is stronger in SNe Ic than in SNe Ib. Matheson et al. (2001) used fractional line depth (i.e., the line depth with respect to the corresponding continuum) to quantify the strength of absorption features. They found that the fractional line depth of O I λ7774 increases from SNe Ib to SNe Ic. They argued that if the helium envelope dilutes the strength of the oxygen line, this increase in strength of O I λ7774 could indicate a decreasing envelope mass from SNe Ib to SNe Ic. We revisit this question, since compared to the dataset in Matheson et al. (2001), we have in our sample twice and three times more SNe Ib and SNe Ic,[16] respectively. Moreover, we use uncertainty arrays of spectra to calculate the error bars of our measurements, whereas Matheson et al. (2001) estimated the error bars of their measurements to be 10% or 20% of their corresponding measured values.

As discussed in Section 3.2, we use pEW to quantify strength of absorption features. The O I λ7774 pEW values of individual SNe and the corresponding rolling weighted averages are displayed in Figure 11. Although there is a wide overlap in the pEW values between the two SN subtypes, on average, SNe Ic have stronger O I λ7774 than SNe Ib from $t_{\rm Vmax} \simeq -10$ days to $t_{\rm Vmax} \simeq 25$ days. At $t_{\rm Vmax} \simeq 0$, the pEW values of O I λ7774 for individual SNe Ic range from 60 Å to 110 Å, while the pEW values range from 10 Å to 60 Å for individual SNe Ib, except for SN 2009jf, which has pEW values within the range of SNe Ic. We agree with the conclusion in Matheson et al. (2001) that there is an increase in strength of O I λ7774 from SNe Ib to SNe Ic in terms of average values, while having used a larger sample than Matheson et al. (2001) did. Our observations support the predictions of Frey et al. (2013) that SNe Ic have stronger O I λ7774 than SNe Ib, though the new mixing algorithm used in Frey et al. (2013) needs to be verified. However, under certain assumptions, our observations contradict predictions made by Dessart et al. (2012) that SNe Ib have stronger lines than SNe Ic, if the only difference between SNe Ib and SNe Ic had been the level of mixing. This indicates that progenitors of SNe Ic may not contain helium before the explosion, i.e., the mixing is not the only difference between SNe Ib and SNe Ic, as also supported by our Fe II λ5169 and O I λ7774 velocity measurements (see the section below).

We note that if the progenitors of SNe Ic have larger core masses than those of SNe Ib, SNe Ic could have helium in their envelopes that will not be excited (i.e., they could have "hidden" helium), and at the same time, show stronger O I λ7774 than SNe Ib, since even for efficient mixing, a star with a more massive CO core will not be able to produce a SN Ib because too little ^{56}Ni will be mixed into the outer layers of the ejecta (Dessart et al. 2015). However, various works have shown that SNe Ib and SNe Ic have similar ejecta masses (e.g., Drout et al. 2011; Lyman et al. 2014, Bianco et al. in prep), indicating that SNe Ib and SNe Ic may have comparable CO cores before explosion. Thus, our observation that SNe Ic have stronger O I λ7774 than SNe Ib may not be due to a more massive CO core in SN Ic progenitors. We conclude that progenitors of SNe Ic may not contain helium before the explosion. Moreover, Hachinger et al. (2012) show that based on their non-LTE radiative transfer models, SNe Ic cannot hide more than 0.06 $M_\odot$ of helium. In the next section, we will explore this topic further with another observational indicator.

5.2.2. *Absorption Velocity of Fe II λ5169 and O I λ7774*

Using non-LTE radiative transfer calculations, Dessart et al. (2012) argued that if SNe Ib and SNe Ic have the same progenitors but SNe Ib have a higher mixing level, (i.e., the progenitors of SNe Ic have the helium layers but insufficient ^{56}Ni mixing), SNe Ib will

[15] The strength of the Fe II λ5169 line is also an ideal indicator to test the predictions of Dessart et al. (2012), since iron should have a uniform mass fraction through most of the ejecta during the photospheric phase. However, the Fe II λ5169 strength is not easy to measure since the local continuum is difficult to define due to the appreciable difference between the height of the two local maxima around the absorption line.

[16] We only include the subset of SNe Ib and Ic whose spectra cover the O I λ7774 absorption feature.

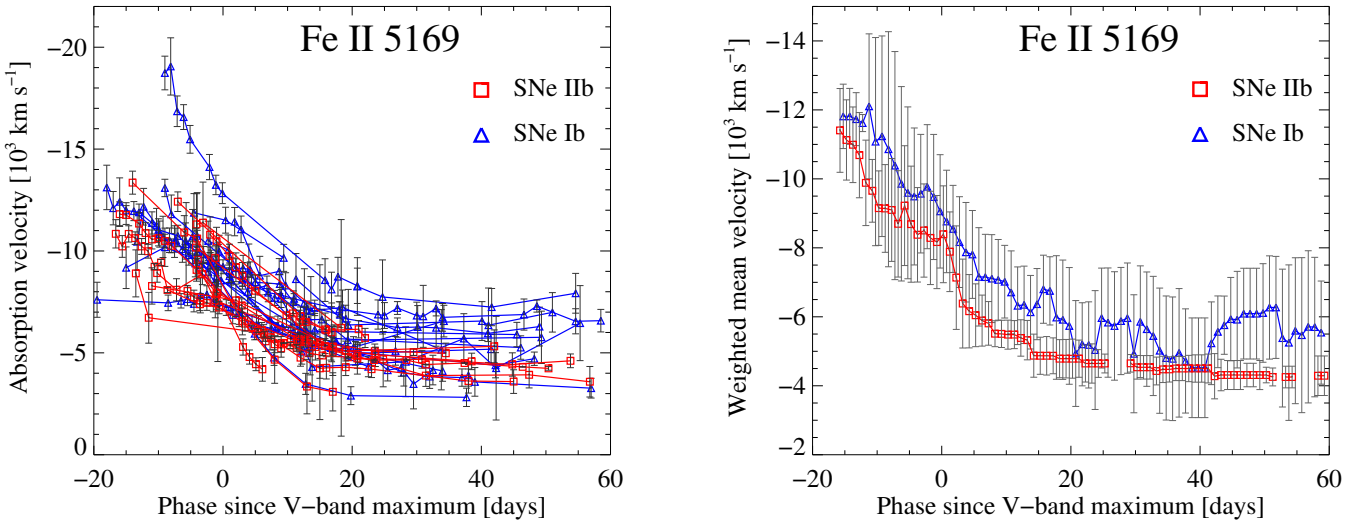

Figure 8. The same as Figure 2, but for measurements of Fe II λ5169 velocities.

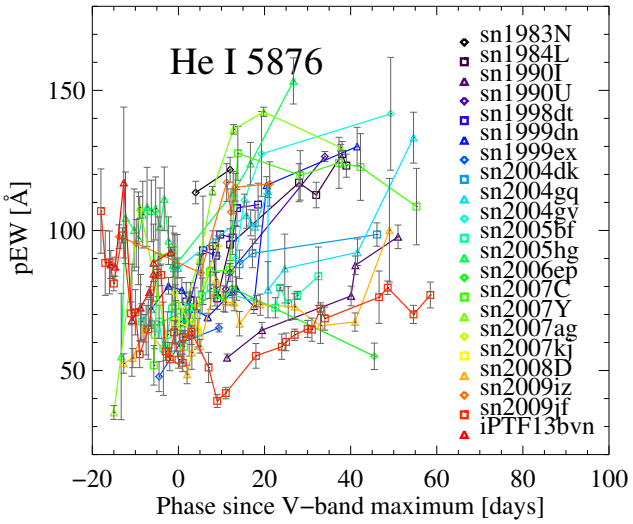

Figure 9. Measurements of He I λ5875 pEW values for each SN Ib in our sample. Data points of the same SN are connected by a line.

have higher photospheric velocities than SNe Ic. That is because with more mixing, there will be more opacity due to metals, thus the photosphere, where the optical depth is $\tau = 2/3$, will be farther out. We test this prediction by measuring the absorption velocity of Fe II λ5169 and O I λ7774 in a statistically significant set of SNe Ib and Ic, since they are suggested to trace the velocity at the photosphere by Branch et al. (2002) and Dessart et al. (2015),[17] respectively.

Figure 7 in Section 4.5 shows our phenomenological method to identify Fe II $\lambda\lambda\lambda$4924, 5018, and 5169. Given that Fe II $\lambda\lambda$4924 and 5018 are usually blended together, here we report the velocities of Fe II λ5169 as

[17] See Dessart et al. (2015) and Modjaz et al. (2015) for discussions on what the definition of "photospheric" velocity is and which line to use.

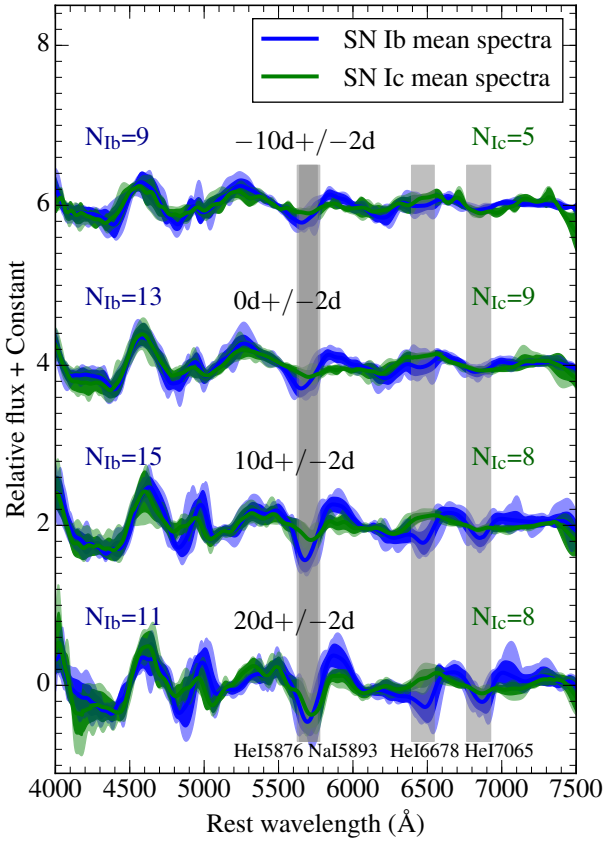

Figure 10. The same as Figure 1, but for SNe Ib (blue) and SNe Ic (green). N_{Ib} represents the number of spectra or SNe that go into each mean spectrum of SNe Ib, and N_{Ic} represents the number for SNe Ic. The gray vertical bands indicate the expected positions of He I λ5876, Na I D, He I $\lambda\lambda$ 6678, and 7065 at velocities of -6000 km s^{-1} to -13000 km s^{-1}.

the photospheric velocities. We emphasize that even if the Fe II λ5169 feature we identified is not due to Fe, our relative comparisons are still valuable since we measure the same feature in the same way. The Fe II λ5169 velocities and O I λ7774 velocities of both individual SNe

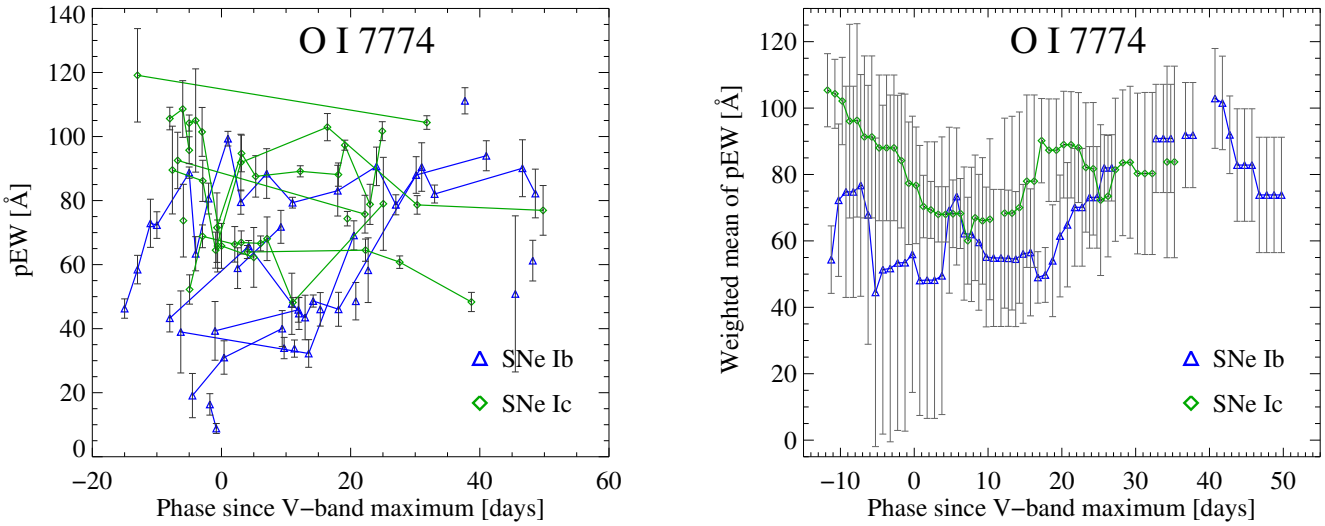

Figure 11. The same as Figure 2, but for measurements of O I λ7774 pEW for SNe Ib (blue triangles) and SNe Ic (green diamonds). In the left panel, the SN Ib that falls within the SN Ic sample at $t_{\rm Vmax} \simeq 0$ day is SN 2009jf.

Table 7
Summary of weighted average of the measurements for SNe Ib and Ic at $t_{\rm Vmax} \simeq 0$ day

SN type	pEW (O I λ7774) (Å)	v (Fe II λ5169) (km s^{-1})	v (O I λ7774) (km s^{-1})
SNe Ib	56 ± 42	−9100 ± 1600	−8400± 300
SNe Ic	77 ± 18	−11000 ± 3700	−13600 ± 4300

Note. — The error is the standard deviation of data that contribute the weighted average value, which is consistent with the errors in the figures that show weighted average values.

and the corresponding rolling weighted averages are displayed in Figure 12. Although at any given epoch, the velocity measurements for SNe Ib and Ic are consistent with each other, the weighted average velocities of both Fe II λ5169 and O I λ7774 velocities in SNe Ic are systematically higher than those in SNe Ib at all epochs. This observation is inconsistent with the predictions of Dessart et al. (2012). Therefore, the progenitors of SNe Ib and SNe Ic should be different not only in the mixing level of ^{56}Ni but also in their composition. Since we have good reasons to believe that the ejecta masses of SNe Ib and SNe Ic are comparable (e.g., Drout et al. 2011; Lyman et al. 2014, Bianco et al. in prep), the progenitors of SNe Ib and SNe Ic may have identical CO cores. Thus, we conclude that the difference between progenitors of SNe Ib and SNe Ic may lie in the outer layers, i.e., SN Ic progenitors may have a very thin or absent helium layer.

Table 7 lists the weighted average of our observations for SNe Ib and SNe Ic at $t_{\rm Vmax} \simeq 0$ day.

6. USING MEAN SPECTRA AND THEIR CORRESPONDING STANDARD DEVIATIONS TO CHARACTERIZE SPECTRAL DIVERSITY

Mean spectra and the standard deviations from the mean characterize the spectral diversity of each SN subtype, thus they can be used to determine if a newly discovered SN belongs to an already known subtype, or is a novel discovery. With the large amount of data we have, we construct mean spectra and their corresponding standard deviations as a function of subtype and phase. To reduce the effect of reddening, these mean spectra are constructed from continuum-divided spectra.

In Figures 13 and 14, we show the mean spectra, one standard deviation from the mean, and the ratio of the standard deviation to the mean for SNe IIb, SNe Ib and SNe Ic at $t_{\rm Vmax} = -10$, 0, and 10 days. The mean spectra and their corresponding standard deviation for SNe Ic-bl are published in Modjaz et al. (2015). Although the spectral diversity of SN features are already shown in previous figures, such as Figure 2, now we can directly observe the spectral diversity of different stripped SN classes via their mean spectra and the corresponding standard deviations. For the mean spectra of SNe Ib (Figure 14), the deepest absorption feature is due to He I λ5876 with possible contamination from Na I D. Other two obvious features are produced by He I λλ6678 and 7065. These three lines evolve to lower velocities but grow stronger as time goes by. The above velocity evolution is expected since the velocity scales with radius in homologous expansion and the photosphere—where the absorption features are produced—recedes towards the center of the expansion as time elapses. For the mean spectra of SNe IIb (Figure 13), the strongest absorption feature is due to Hα, which becomes weaker with time. Other three prominent absorption troughs in SNe IIb are attributed to He I λλλ5876, 6678, and 7065, whose velocity evolutions and strength evolutions behave similarly to those in the mean spectra of SNe Ib. These trends are confirmed by velocity and pEW measurements of Hα and He I lines for individual SNe in Figures 2, 3, and 6.

We test whether the so-called "prototypical" SN IIb 1993J is truly representative of SNe IIb by comparing its spectra with our mean spectra of SNe IIb. As shown in Figure 13, SN 1993J is fully consistent with the mean spectra of SNe IIb, except for the Hα absorption feature at phase $t_{\rm Vmax} = 10$ days. Thus, SN 1993J is a typical SN IIb from a spectroscopic point of view.

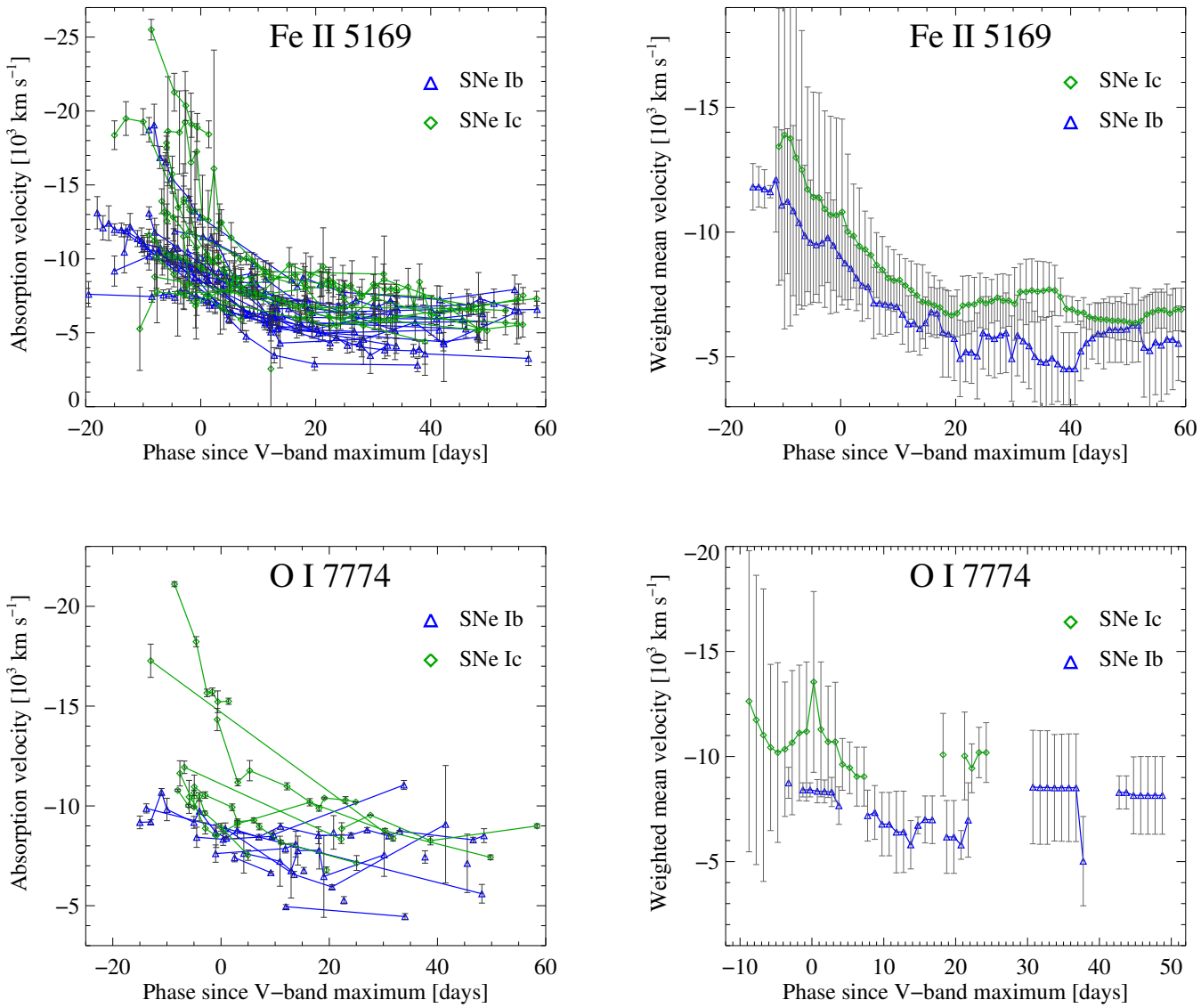

Figure 12. The same as Figure 2, but for measurements of Fe II λ5169 velocities (*Top*) and O I λ 7774 velocities (*Bottom*) for SNe Ib (blue triangles) and SNe Ic (green diamonds).

The ratio between the standard deviation and the mean spectra in the right panels of Figures 13 and 14 show that in most cases, the spectra of SNe IIb, SNe Ib, and SNe Ic are within 20% of the corresponding mean spectrum. The spectral variance is relatively small at $t_{\rm Vmax} = -10$ and 0 days, but relatively large around the absorption features. For example, the spectral variance around He I lines in the mean spectra of SNe IIb and SNe Ib is larger than that at other wavelengths. For the mean spectra of SNe IIb, the spectral variance is also large around the Hα and Hβ features. This indicates that there is a diversity in the thickness of either the helium or hydrogen layers (or both) of the progenitors.

In Figure 15, we show how our average spectra can be used to discover and study relatively novel SN types such as Calcium-rich Type Ib SNe (SNe Ib-Ca; Filippenko et al. 2003; Perets et al. 2010; Kasliwal et al. 2012). Compared to SNe Ib, whose spectroscopic hallmark is the prominent He I lines, SNe Ib-Ca also display unusually strong lines of calcium during their nebular phase. Although the origin of SNe Ib-Ca is contentious (Perets et al. 2010; Meng & Han 2015), in Figure 15 we spectroscopically compare the SN Ib-Ca 2005E (Perets et al. 2010) to our SN Ib average spectra. The velocities and strengths of He I lines in the spectra of SN 2005E are consistent with those of the average SN Ib spectra at comparable phases. At $t_{\rm Vmax} \simeq 65$ days, SN 2005E exhibits a much stronger Ca emission line around 7300 Å than the SN Ib average spectrum. We also note that at $t_{\rm Vmax} \simeq 10$ days, the Fe II lines around 5000 Å in the SN 2005E spectrum form a "v"-like feature (which is commonly seen in SNe Ic-bl), instead of the "w"-like feature that appears in SNe Ib (as well as in SNe IIb and SNe Ic). Thus, instead of comparing newly discovered SNe to individual SNe with a known type, comparing the new SNe to our average spectra of different SN sub-

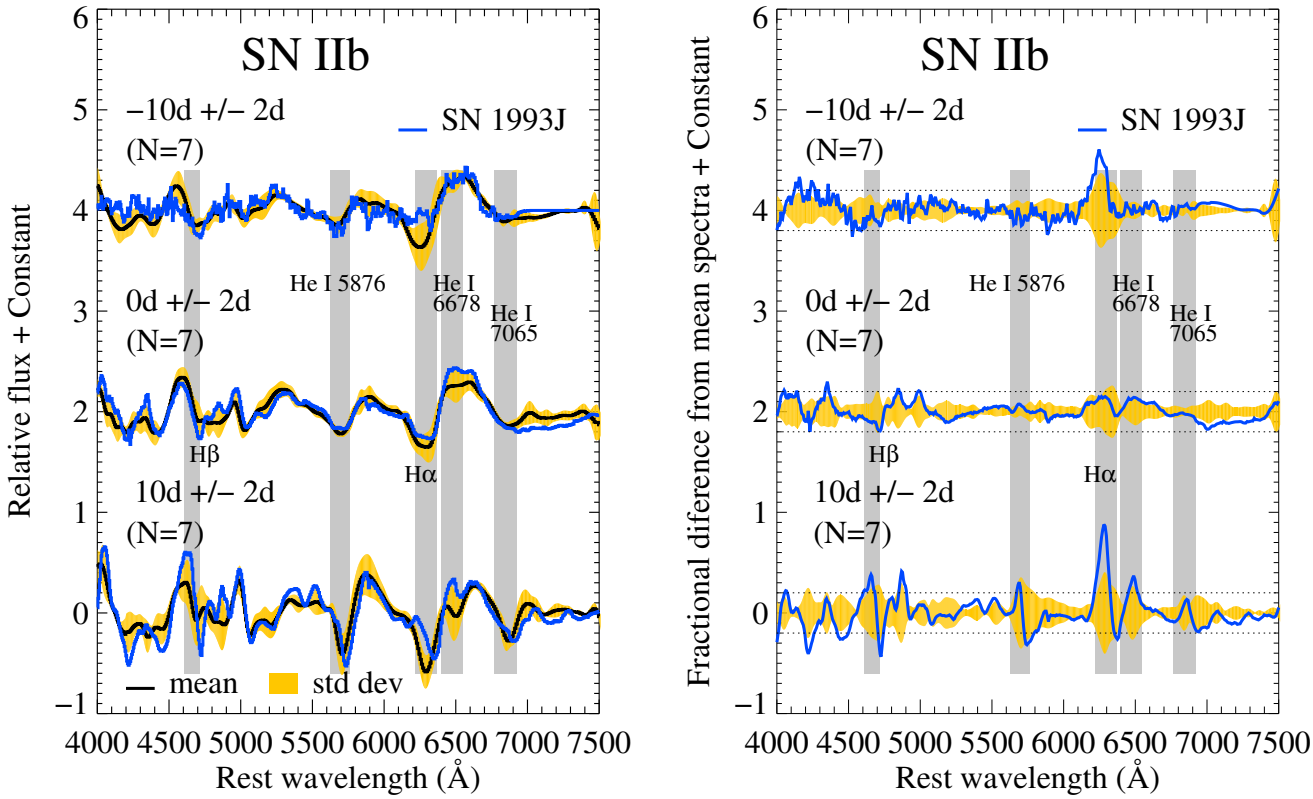

Figure 13. *Left*: Mean spectra of SNe IIb (in black) with corresponding standard deviations (in yellow) at phase ranges: -10 $(+/-2)$ days (top), 0 $(+/-2)$ days (middle), and 10 $(+/-2)$ days (bottom). In blue, we show the flattened (or continuum-divided) spectra of SN 1993J at $t_{\rm Vmax} \simeq -11$, 1, and 11 days. *Right*: The standard deviation of the mean spectrum divided by the mean spectrum is shown in yellow. For comparison, the difference between the SN 1993J spectrum and the mean spectrum, also divided by the mean spectrum, is shown in blue. Dotted horizontal lines represent the 20% of the mean spectrum. The number of spectra used to build each mean spectrum is shown in parentheses. The gray vertical bands indicate the expected positions of He I $\lambda\lambda$5876, 6678, and 7065 at velocities of -6000 km s^{-1} to -13000 km s^{-1}, or the expected positions of Hα and Hβ at velocities of -9000 km s^{-1} to -16000 km s^{-1}.

types is more powerful for detecting spectroscopically novel SNe (though they may also have photometric differences).

7. SUMMARY AND CONCLUSIONS

In this paper, we have improved the SN identification scheme and constrained the progenitors of different kinds of stripped SNe by analyzing the spectra of the largest stripped SN sample (which consists of 242 spectra of 14 SNe IIb, 262 spectra of 21 SNe Ib, and 207 spectra of 17 SNe Ic) in a statistical and quantitative way. To be thorough, we have derived robust error bars for velocity and pEW measurements by constructing uncertainty arrays from the SN spectra themselves (by separating noise from SN signal in Fourier space) for the very first time and then propagating those uncertainties into our final measurements via MC simulations.

To better classify SNe IIb and Ib, we have quantified the properties of spectral features by measuring absorption velocity and pEW values of Hα, He I $\lambda\lambda$5876, 6678, 7065, and Fe II λ5169. We then compared these values for SNe IIb with those for SNe Ib in a statistical way. On the one hand, there is substantial overlap in almost all of our above measurements, suggesting an observational continuum between SNe IIb and Ib. The observational continuum is most likely due to a continuum of sizes or masses of the hydrogen or helium layers. On the other hand, the Hα pEW values of SNe Ib are different from those of SNe IIb at all phases, which can be used to classify these two SN subtypes. Although there is no clear boundary between the pEW values of Hα for the SN IIb sample and those for the SN Ib sample, there is no overlap at any phase. Thus if a SN is identified as a SN IIb once, it remains a SN IIb. Therefore, the Hα pEW value can be used to differentiate SNe IIb from SNe Ib at all epochs. We suggest that to classify a new SN IIb/Ib, not only the spectroscopic SN identification tools (e.g., SNID, GELATO[18]) should be used, but also the properties (e.g., Hα pEW values) of the new SN IIb/Ib should be measured, announced, and compared to SNe IIb and Ib described here.

We have addressed the question of hidden helium in SNe Ic by comparing our observations of O I λ7774 strength, Fe II λ5169 velocity, and O I λ7774 velocity for SNe Ib and Ic with theoretical predictions. Table 8 summarizes these comparisons. We find that on average, SNe Ib have higher photospheric velocities (as traced by Fe II λ5169 velocities) than SNe Ic, which is inconsistent with the predictions of Dessart et al. (2012) based on a hidden helium model for SN Ic progenitors, **if the only**

[18] https://gelato.tng.iac.es/

Table 8
Summary of comparisons between our observations and predictions as well as other observations in the literature

Absorption Feature	Our Observation	M01[a]	D12[b]	F13[c]
O I λ7774	$pEW_{Ic} > pEW_{Ib}$	consistent	inconsistent	consistent
Fe II λ5169	$V_{Ic} > V_{Ib}$	NA	inconsistent	NA
O I λ7774	$V_{Ic} > V_{Ib}$	NA	inconsistent	NA

[a] M01 = Matheson et al. (2001)
[b] D12 = Dessart et al. (2012)
[c] F13 = Frey et al. (2013)

difference between SN Ib and SN Ic progenitors were the level of 56Ni mixing. Furthermore, we find that the average pEW values of O I λ7774 for SNe Ic are stronger than those for SNe Ib, which supports predictions of Frey et al. (2013) based on a helium-free model for SN Ic progenitors, though the new mixing algorithm used in Frey et al. (2013) needs to be verified. This indicates that progenitors of SNe Ic may not contain helium before the explosion. **The same conclusion has been reached in ? using early time light curves of stripped SNe.**

We have constructed continuum-divided mean spectra and their corresponding standard deviation arrays for SNe IIb, SNe Ib, and SNe Ic to characterize their respective spectral diversity, which show systematic differences between SN subtypes. These mean spectra should be used in discovery of spectroscopically novel SNe and spectroscopic classification of SNe. By comparing the spectra of SN 1993J with the SN IIb mean spectra, we show that SN 1993J is a typical SN IIb from a spectroscopic point of view. We also find that the spectral diversity is relatively large around absorption features such as He I lines and H lines, which should be taken into account when progenitor models are coupled to spectral synthesis codes.

For convenience, we summarize the trends we observe in our sample, which may help constrain the progenitor models of SNe IIb, SNe Ib and SNe Ic:

- Average velocities of Hα, He I $\lambda\lambda\lambda$5876, 6678, 7065, and Fe II λ5169 in SNe Ib are systematically higher than those in SNe IIb.
- The Hα pEW values in SNe IIb are systematically higher than those in SNe Ib at all phases.
- The He I $\lambda\lambda$5876, 6678 velocities in most SNe IIb and Ib decrease rapidly over time while the He I λ7065 velocities only decrease slightly.
- SNe IIb and Ib have comparable pEW values of He I λ5876. On average, SNe Ib have larger pEW values of He I λ6678 than SNe IIb. The He I λ7065 pEW values are comparable in SNe IIb and Ib before $t_{\rm Vmax} \simeq 10$ days. However, SNe IIb show much stronger He I λ7065 than SNe Ib at later epochs.
- Three SNe IIb and four SNe Ib in our sample have flat-velocity He I lines while none of them show flat-velocity Fe II λ5169 line.
- On average, SNe Ic have stronger O I λ7774 than SNe Ib from $t_{\rm Vmax} \simeq -10$ days to $t_{\rm Vmax} \simeq 25$ days.
- The average Fe II λ5169 velocities and O I λ7774 velocities in SNe Ic are systematically higher than those in SNe Ib.
- The average Fe II λ5169 velocities are highest for SNe Ic, followed by SNe Ib, and finally by SNe IIb, which systematically have the lowest average Fe II λ5169 velocities.
- For all SN subtypes, the spectral variance is larger around absorption features such as H lines and He I lines than at other wavelengths.

Both asphericity and intrinsic diversity will contribute to the diversity within a subset, and the spectral diversity within the observable sample of SNe IIb is comparable to the degree of asymmetry observed in galactic SN IIb Cassiopeia A, as probed by light echo spectra (**?**). However the systematic spectral trend as a function of subtype (e.g., on average, SNe Ic having the highest Fe II velocities, vs. SNe IIb having the lowest) is then unlikely to be explained with asphericity alone. Future radiative transfer calculations that aim to elucidate the nature of SNe IIb, Ib, and Ic need to reproduce the many observed trends that have been presented here. In order to complete the sequence of massive star explosions, the measured absorption velocities and pEW values for Hα in SNe IIb and Ib should be compared with those in SNe II. We suggest the use of realistic non-LTE codes that properly treat non-thermal excitations to explore all our SN Ic spectra for the presence of He I lines. The spectral diversity in stripped SNe should be explored further using machine-learning methods. In order to be used in the photometric SN classifiers (e.g., Poznanski et al. 2002), mean spectra that retain the continuum information, include more SN spectra, sampled at a smaller phase bin, and cover a longer wavelength range should be constructed for different types of SNe.

The mean spectra and new SNID templates produced in this study can be downloaded via our SNYU webpage.[19]

We are grateful to Luc Dessart, Ross Fadely, Lluis Galbany, Avishay Gal-Yam, David W. Hogg, Dan Milisavljevic, Jerod Parrent, Nathan Smith, and Sung-Chul Yoon for useful discussions. We thank Stephane Blondin for making available to us the codes from Blondin & Tonry (2007) and Blondin et al. (2011) to measure absorption velocities and pEW, as well as to produce mean spectra.

[19] http://cosmo.nyu.edu/SNYU/spectra

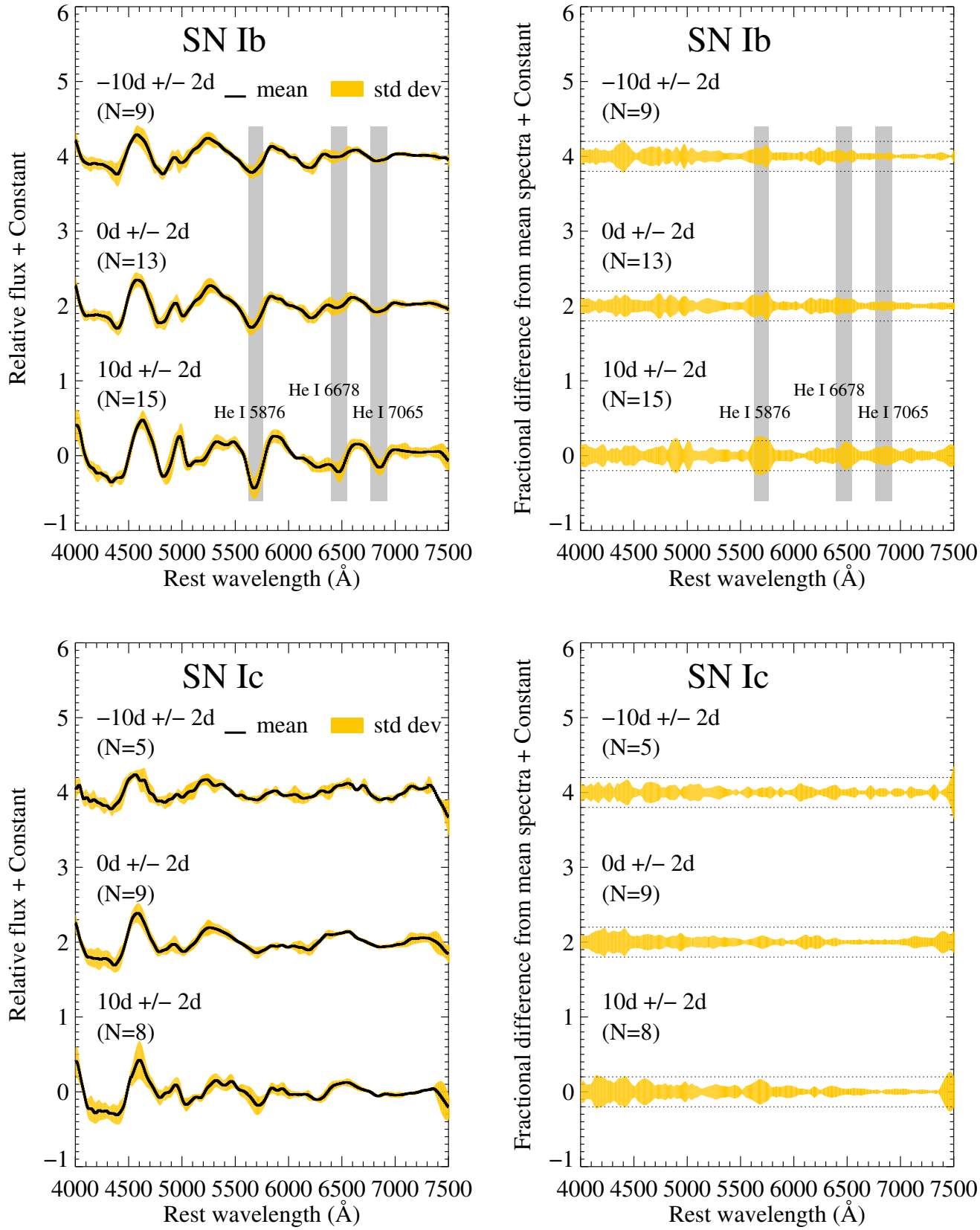

Figure 14. Same as Figure 13, but for SNe Ib and Ic.

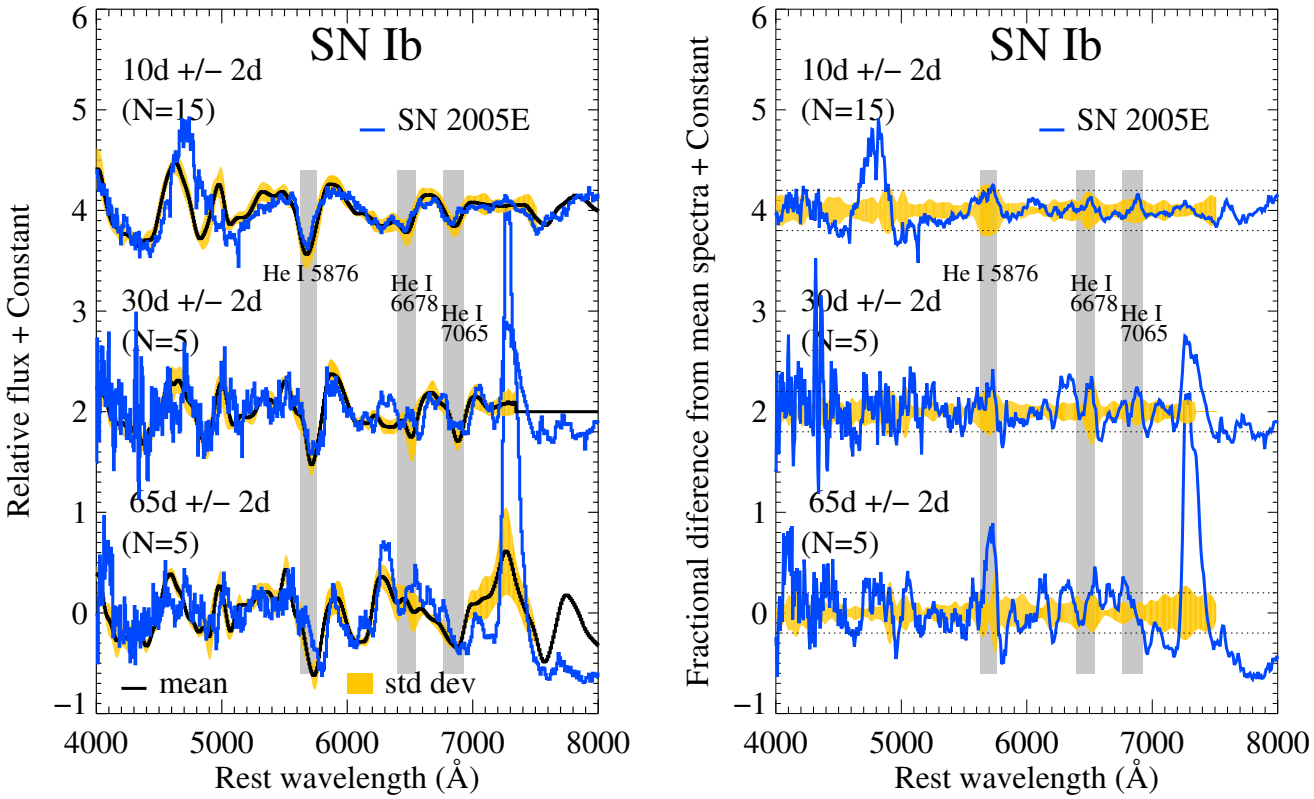

Figure 15. The same as Figure 13, but for the comparison between normal SN Ib and SN Ib-Ca 2005E. The spectra of SN 2005E are at $t_{\rm Vmax} \simeq 11$, 31, and 65 days.

Y.-Q. Liu is supported in part by a NYU/CCPP James Arthur Graduate Fellowship. M. Modjaz and the SNYU group are supported by the NSF CAREER award AST-1352405 and by the NSF award AST-1413260. F. Bianco is supported in part by the NYU/CCPP James Arthur Postdoctoral Fellowship.

This research has made use of NASA's Astrophysics Data System Bibliographic Services (ADS), the HyperLEDA database and the NASA/IPAC Extragalactic Database (NED) that is operated by the Jet Propulsion Laboratory, California Institute of Technology, under contract with the National Aeronautics and Space Administration.

REFERENCES

Abbott, D. C., & Lucy, L. B. 1985, ApJ, 288, 679
Arcavi, I., Gal-Yam, A., Yaron, O., et al. 2011, ApJ, 742, L18
Babu, G. J., & Feigelson, E. D. 2006, in Astronomical Society of the Pacific Conference Series, Vol. 351, Astronomical Data Analysis Software and Systems XV, ed. C. Gabriel, C. Arviset, D. Ponz, & S. Enrique, 127
Babu, G. J., & Singh, K. 1983, Ann. Statist., 11, 999
Barbon, R., Benetti, S., Cappellaro, E., et al. 1995, A&AS, 110, 513
Barbon, R., Benetti, S., Rosino, L., Cappellaro, E., & Turatto, M. 1990, A&A, 237, 79
Benetti, S., Turatto, M., Valenti, S., et al. 2011, MNRAS, 411, 2726
Bianco, F. B., Modjaz, M., Hicken, M., et al. 2014, ArXiv:1405.1428, arXiv:arXiv:1405.1428
Blondin, S., Mandel, K. S., & Kirshner, R. P. 2011, A&A, 526, A81
Blondin, S., & Tonry, J. L. 2007, ApJ, 666, 1024
Blondin, S., et al. 2006, AJ, 131, 1648
Bloom, J. S., Kasen, D., Shen, K. J., et al. 2012, ApJ, 744, L17
Branch, D., Jeffery, D. J., Young, T. R., & Baron, E. 2006, PASP, 118, 791
Branch, D., Benetti, S., Kasen, D., et al. 2002, ApJ, 566, 1005
Burrows, A. 2013, Reviews of Modern Physics, 85, 245
Cao, Y., et al. 2013, ApJ, 775, L7
Clocchiatti, A. 2000, ApJ, 529, 661
Clocchiatti, A., Wheeler, J. C., Brotherton, M. S., et al. 1996, ApJ, 462, 462
Clocchiatti, A., et al. 1997, ApJ, 483, 675
Deng, J. S., Qiu, Y. L., Hu, J. Y., Hatano, K., & Branch, D. 2000, ApJ, 540, 452
Dessart, L., Hillier, D. J., Li, C., & Woosley, S. 2012, MNRAS, 424, 2139
Dessart, L., Hillier, D. J., Livne, E., et al. 2011, MNRAS, 414, 2985
Dessart, L., Hillier, D. J., Woosley, S., et al. 2015, ArXiv e-prints, arXiv:1507.07783
Drout, M. R., Soderberg, A. M., Gal-Yam, A., et al. 2011, ApJ, 741, 97
Elmhamdi, A., Danziger, I. J., Branch, D., et al. 2006, A&A, 450, 305
Elmhamdi, A., Danziger, I. J., Cappellaro, E., et al. 2004, A&A, 426, 963
Ergon, M., Sollerman, J., Fraser, M., et al. 2014, A&A, 562, A17
Filippenko, A. V. 1997, ARA&A, 35, 309
Filippenko, A. V., Chornock, R., Swift, B., et al. 2003, IAU Circ., 8159, 2
Filippenko, A. V., Matheson, T., & Ho, L. C. 1993, ApJ, 415, L103+
Filippenko, A. V., et al. 1995, ApJ, 450, L11+
Folatelli, G., Contreras, C., Phillips, M. M., et al. 2006, ApJ, 641, 1039

Folatelli, G., Bersten, M. C., Kuncarayakti, H., et al. 2014, ApJ, 792, 7
Fransson, C., Challis, P. M., Chevalier, R. A., et al. 2005, ApJ, 622, 991
Fremling, C., Sollerman, J., Taddia, F., et al. 2014, A&A, 565, A114
Frey, L. H., Fryer, C. L., & Young, P. A. 2013, ApJ, 773, L7
Gal-Yam, A. 2012, Science, 337, 927
Graur, O., & Maoz, D. 2013, MNRAS, 430, 1746
Hachinger, S., Mazzali, P. A., Taubenberger, S., et al. 2012, MNRAS, 422, 70
Hamuy, M., Maza, J., Pinto, P. A., et al. 2002, AJ, 124, 417
Hamuy, M., Deng, J., Mazzali, P. A., et al. 2009, ApJ, 703, 1612
Hauschildt, P. H., & Baron, E. 1999, Journal of Computational and Applied Mathematics, 109, 41
—. 2004, A&A, 417, 317
Homeier, N. L. 2005, ApJ, 620, 12
Horne, K. 1986, PASP, 98, 609
Iwamoto, K., Nakamura, T., Nomoto, K., et al. 2000, ApJ, 534, 660
James, S., & Baron, E. 2010, ApJ, 718, 957
Jeffery, D. J., Kirshner, R. P., Challis, P. M., et al. 1994, ApJ, 421, L27
Jones, D. O., Rodney, S. A., Riess, A. G., et al. 2013, ApJ, 768, 166
Kasliwal, M. M., Kulkarni, S. R., Gal-Yam, A., et al. 2012, ApJ, 755, 161
Kumar, B., Pandey, S. B., Sahu, D. K., et al. 2013, MNRAS, 431, 308
Langer, N. 2012, ARA&A, 50, 107
Liu, Y. Q., & Modjaz, M. 2014, ArXiv:1405.1437, arXiv:arXiv:1405.1437
Lucy, L. B. 1991, ApJ, 383, 308
—. 1999, A&A, 345, 211
Lyman, J., Bersier, D., James, P., et al. 2014, ArXiv e-prints, arXiv:1406.3667
Malesani, D., Fynbo, J. P. U., Hjorth, J., et al. 2009, ApJ, 692, L84
Maoz, D., Mannucci, F., & Nelemans, G. 2014, ARA&A, 52, 107
Marion, G. H., Vinko, J., Kirshner, R. P., et al. 2014, ApJ, 781, 69
Matheson, T., Filippenko, A. V., Ho, L. C., Barth, A. J., & Leonard, D. C. 2000a, AJ, 120, 1499
Matheson, T., Filippenko, A. V., Li, W., Leonard, D. C., & Shields, J. C. 2001, AJ, 121, 1648
Matheson, T., et al. 2000b, AJ, 120, 1487
Mazzali, P. A. 2000, A&A, 363, 705
Mazzali, P. A., Deng, J., Hamuy, M., & Nomoto, K. 2009, ApJ, 703, 1624
Mazzali, P. A., & Lucy, L. B. 1993, A&A, 279, 447
Mazzali, P. A., Valenti, S., Della Valle, M., et al. 2008, Science, 321, 1185
Meng, X., & Han, Z. 2015, A&A, 573, A57
Milisavljevic, D., Fesen, R. A., Gerardy, C. L., Kirshner, R. P., & Challis, P. 2010, ApJ, 709, 1343
Milisavljevic, D., Margutti, R., Soderberg, A. M., et al. 2013, ApJ, 767, 71
Modjaz, M., Liu, Y. Q., Bianco, F. B., & Graur, O. 2015, ArXiv e-prints, arXiv:1509.07124
Modjaz, M., Li, W., Butler, N., et al. 2009, ApJ, 702, 226
Modjaz, M., Blondin, S., Kirshner, R. P., et al. 2014, AJ, 147, 99
Moskvitin, A. S., Sonbas, E., Sokolov, V. V., Fatkhullin, T. A., & Castro-Tirado, A. J. 2010, Astrophysical Bulletin, 65, 132
Nomoto, K., Iwamoto, K., & Suzuki, T. 1995, Phys. Rep., 256, 173
Nugent, P. E., Sullivan, M., Cenko, S. B., et al. 2011, Nature, 480, 344
Oates, S. R., Bayless, A. J., Stritzinger, M. D., et al. 2012, MNRAS, 424, 1297
Parrent, J., Branch, D., & Jeffery, D. 2010, SYNOW: A Highly Parameterized Spectrum Synthesis Code for Direct Analysis of SN Spectra, Astrophysics Source Code Library, ascl:1010.055
Parrent, J., Branch, D., Troxel, M. A., et al. 2007, PASP, 119, 135
Parrent, J. T., Milisavljevic, D., Soderberg, A. M., & Parthasarathy, M. 2015, ArXiv e-prints, arXiv:1505.06645
Pastorello, A., Smartt, S. J., Mattila, S., et al. 2007, Nature, 447, 829
Pastorello, A., Prieto, J. L., Elias-Rosa, N., et al. 2015, MNRAS, 453, 3649
Perets, H. B., Gal-Yam, A., Mazzali, P. A., et al. 2010, Nature, 465, 322
Podsiadlowski, P., Langer, N., Poelarends, A. J. T., et al. 2004, ApJ, 612, 1044
Poznanski, D., Gal-Yam, A., Maoz, D., et al. 2002, PASP, 114, 833
Poznanski, D., Chornock, R., Nugent, P. E., et al. 2010, Science, 327, 58
Press, W. H., Teukolsky, S. A., Vetterling, W. T., & Flannery, B. P. 2007, Numerical Recipes 3rd Edition: The Art of Scientific Computing, 3rd edn. (New York, NY, USA: Cambridge University Press)
Quimby, R. M., Kulkarni, S. R., Kasliwal, M. M., et al. 2011, Nature, 474, 487
Richmond, M. W., et al. 1996, AJ, 111, 327
Rodney, S. A., Riess, A. G., Scolnic, D. M., et al. 2015, ArXiv e-prints, arXiv:1508.03100
Sahu, D. K., Gurugubelli, U. K., Anupama, G. C., & Nomoto, K. 2011, MNRAS, 383
Sauer, D. N., Mazzali, P. A., Deng, J., et al. 2006, MNRAS, 369, 1939
Silverman, J. M., Kong, J. J., & Filippenko, A. V. 2012a, MNRAS, 425, 1819
Silverman, J. M., Foley, R. J., Filippenko, A. V., et al. 2012b, MNRAS, 425, 1789
Stoll, R., Prieto, J. L., Stanek, K. Z., et al. 2011, ApJ, 730, 34
Stritzinger, M., Mazzali, P., Phillips, M. M., et al. 2009, ApJ, 696, 713
Tominaga, N., et al. 2005, ApJ, 633, L97
Tsvetkov, D. Y., Volkov, I. M., Sorokina, E., et al. 2012, Peremennye Zvezdy, 32, 6
Valenti, S., Fraser, M., Benetti, S., et al. 2011, MNRAS, 416, 3138
Woosley, S. E., Heger, A., & Weaver, T. A. 2002, Reviews of Modern Physics, 74, 1015
Woosley, S. E., Langer, N., & Weaver, T. A. 1993, ApJ, 411, 823
Yaron, O., & Gal-Yam, A. 2012, PASP, 124, 668
Yoon, S.-C., Gräfener, G., Vink, J. S., Kozyreva, A., & Izzard, R. G. 2012, A&A, 544, L11
Yoon, S.-C., & Langer, N. 2005, A&A, 443, 643
Yoon, S.-C., Woosley, S. E., & Langer, N. 2010, ApJ, 725, 940

APPENDIX

A. SPECTRAL PRE-PROCESSING

We need both a flattened (i.e., continuum-divided) version and an original (i.e., continuum-included) version for all of the spectra in our SN sample, for different purposes. The former is used to construct mean spectra for different SN types as a function of phase. The latter is used to measure velocity and strength of absorption features.

Some spectra in our sample are original spectra, while others are continuum-divided spectra. The latter are the SNID templates from the SNID database templates-2.0 (Blondin & Tonry 2007), for which we do not possess the original spectra. The SNID templates are flattened spectra where the continuum has been divided out. We also made some phase and type modifications to these flattened spectra based on Modjaz et al. (2014) and summarized in Liu &

Modjaz (2014). For flattened spectra in our sample, we constructed their "original" spectra by adding the continuum flux (whose information is stored in the SNID template) back to the spectra. The original spectra in our sample contain the continuum, and thus we generated their SNID templates by following the steps in Blondin & Tonry (2007), as well as the instructions on the webpage of SNID.[20] In this manner, we have constructed new SNID templates of all published stripped SN spectra. The SNID templates of the CfA stripped SNe were published in Liu & Modjaz (2014); additional SNID templates of SNe Ic, SNe Ic-bl, and SN-GRBs are published in Modjaz et al. (2015); additional SNID templates of SNe IIb, and SNe Ib are published here.

B. CONSTRUCTING UNCERTAINTY ARRAYS OF SPECTRA

We need to know the uncertainty arrays of spectra to estimate the errors on the velocity and strength measurements, since uncertainty arrays describe the noise level in spectra, which gives rise to the uncertainty in the measurements. Uncertainty arrays are ideally produced during data reduction, in particular during optimal extraction (Horne 1986). The reduction-produced uncertainty arrays mainly include Poisson noise and the readout noise of the CCD. Other sources of noise have a negligible effect on the final uncertainty. The noise varies slowly with wavelength, except at the positions of sky lines or H II region emission lines, so the uncertainty arrays should generally change smoothly with wavelength.

However, most spectra from the literature do not have published reduction-produced uncertainty arrays, nor could we obtain their reduction-produced uncertainty arrays by re-reducing the data, since we do not have the input files (e.g., the raw 2D frames) needed for optimal extraction. Instead, we have developed the following method to derive the uncertainty array from the reduced SN spectrum itself.

We designed an empirical method to filter spectra in Fourier space, where we first separate noise from signal in Fourier space, and then we calculate the uncertainty array as the standard deviations of the noise over a wavelength range. We describe the two steps in detail below, and show them in Figure 16. Methods for producing uncertainty arrays, or spectral filtering have been designed and implemented in the past (e.g., Blondin et al. 2006), including Fourier based filtering methods (e.g., Blondin & Tonry 2007). Unlike its predecessors, however, our method is fully automated: our Fourier filtering algorithm automatically finds the appropriate wave number $k_{\rm noise}$ to separate the signal from the noise for each individual spectrum. This is particularly useful if the goal is, for example, to produce a consistent analysis of large heterogeneous spectral datasets, as in this paper.

Although not periodic, we expect the spectral features to show power in Fourier space at some characteristic scales. We note that in wavelength space, which is the natural space for noise in spectra and is the space for spectra when observed at telescopes, noise is white noise. By definition, white noise has the same power at all wave numbers (k) in Fourier space, so it should be easy to isolate the Fourier components that carry the spectral signal by identifying the wave numbers where the power begins to deviate from a constant, e.g., by looking for the intersection of a power law fit to all Fourier components of a spectrum with a flat-line fit to the ones at large wave numbers (Press et al. 2007). However, the natural space of spectral features is velocity space: the spectral features will have some characteristic sizes when observed in flux-velocity space, and thus some characteristic wave numbers in Fourier space.

The first step of our method is to convert the wavelength axis of a spectrum to velocity space by binning the spectrum on a logarithmic wavelength axis. Since Fourier transform (FT) can be applied to evenly sampled data only, the spectrum in velocity space has to be re-binned (we use a bin size equal to its smallest dispersion), and then the Fast FT algorithm (FFT) is applied. However, by transforming the noise from flux-wavelength space to flux-velocity space and re-binning it, we increase the power at the low wave numbers, so we can no longer treat the noise as white. The low wave numbers are also the wave numbers where the spectral signal has power. The increase in noise power at low wave numbers is marginal compared to the power of the spectral signal, thus the spectral signal still dominates the power at low wave numbers, but there will be a domain where both contribute equally. Our goal is to identify the $k_{\rm noise}$ where the noise begins to have a significant contribution to the power spectrum.

Let us assume that very high and very low velocities are not going to be associated with SN spectral features. Velocities can be converted to wave numbers as $k = c/v$, where c is the speed of light and v is the corresponding velocity. We can safely assume that velocities higher than $\sim 100,000$ km s^{-1} (which corresponds to $k < 3$) or lower than $\sim 1,000$ km s^{-1} (which corresponds to $k > 300$) are not consistent with the velocity of SN spectral features, since none of the SNe in our sample exhibit such extreme velocity widths.

The second step of our method is to fit a power law to the magnitude M ($= \sqrt{P}$, where P is the power of spectrum in Fourier space) for $k > 3$ (to avoid the divergence of M for $k = 0$). Then, since velocities smaller than $1,000$ km s^{-1} are too low for SN features in our sample, we assume that the M for $k > 300$ is entirely due to noise, and calculate the average M for $3 < k < 300$. We find that the $k_{\rm noise}$ corresponds to the intersection of the power law fit and the average M above, which is a good estimate of the wave number that separates spectral signal from the noise. The filtered SN spectrum is then obtained by inverting the FT of the spectrum after suppressing M with $k > k_{\rm noise}$. The filtered SN spectrum is shown in the top panel of Figure 17, and it is the version of the spectrum that we use in the velocity and pEW measurements.

The uncertainty array is obtained by deriving the noise spectrum as the residuals between original spectrum and filtered spectrum, and then calculating the standard deviations of this noise spectrum within a rolling window of 100

[20] http://people.lam.fr/blondin.stephane/software/snid/howto.html

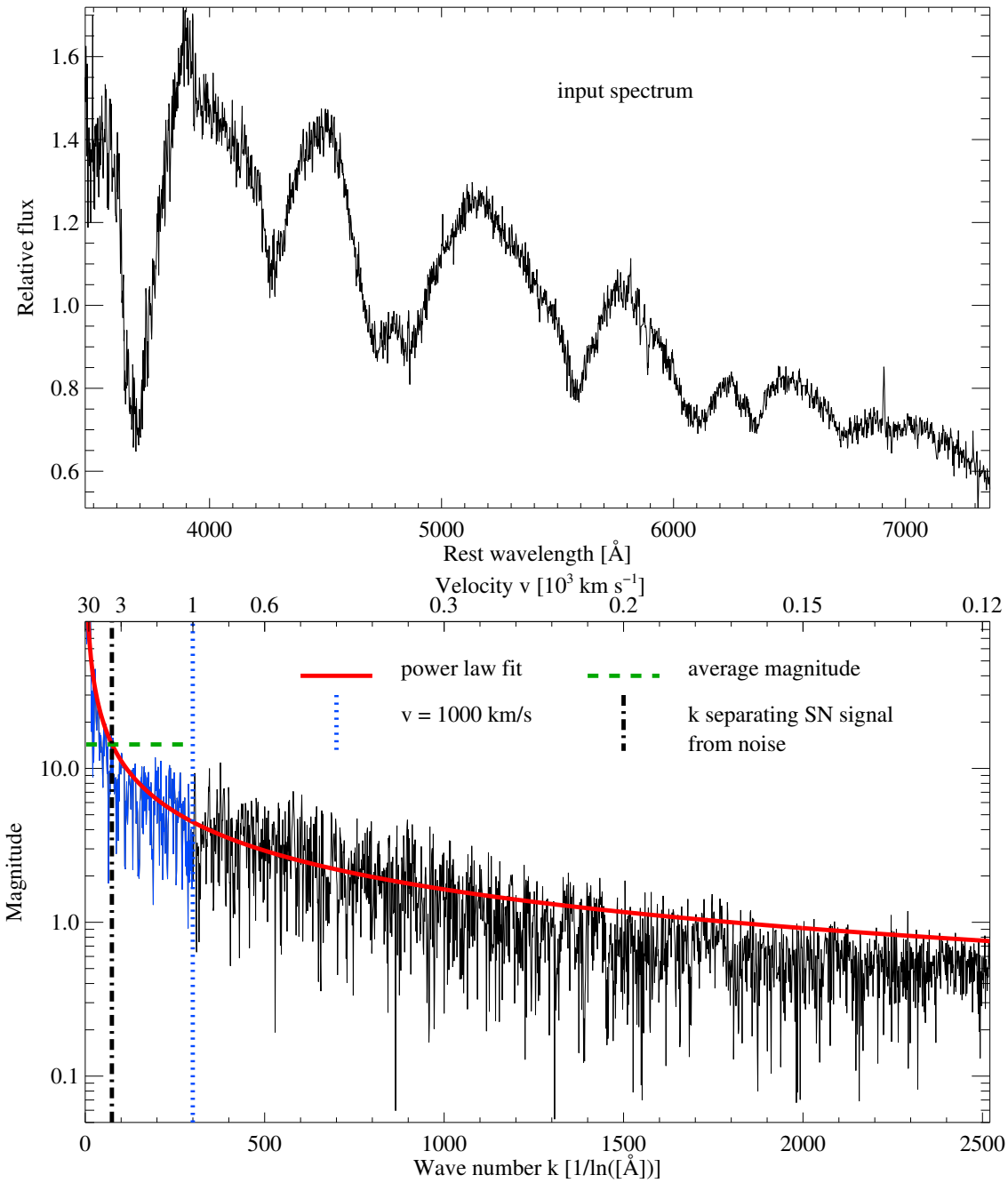

Figure 16. Using Fourier Transform (FT) to separate noise from SN signal in Fourier space and to filter a spectrum. *Upper*: Input spectrum—spectrum of SN Ib SN 2004gq at $t_{\rm Vmax} = -9$ days. *Lower*: FT of the input spectrum (black); A power law fit to magnitudes at wave numbers $k > 3$ is shown in red; Magnitudes corresponding to velocities $1,000 < v < 100,000$ km s^{-1} (or $300 > k > 3$) are shown in blue; Average magnitude of $3 < k < 300$ is shown in green; We identify as noise any FT features at $k > k_{noise}$, where k_{noise} is the intersection (indicated as a black dotted-dashed line) between the above power law fit (red) and the average magnitude (green). In this case, the intersection is at $k = 75$, which corresponds to $v = 4000$ km s^{-1}. The filtered spectrum is generated by inverting the FT after setting the magnitudes for $k > k_{noise}$ to 0 (see the top panel of Figure 17).

Å, a characteristic width for SN features. An example is shown in the middle and bottom panels of Figure 17. Note that since using a rolling window leads to correlated uncertainties the data points in our uncertainty array are not independent.

We find that this method produces uncertainty arrays that are consistent with the reduction-produced ones, having tested this on the subset of the M14 spectra for which reduction-produced uncertainty arrays are available. This subset consists of 28 spectra from nine SNe IIb, nine SNe Ib, and ten SNe Ic. The uncertainty arrays produced with our prescription for all SNe in the sample are within 70%−110% of the ones produced from the optimal extraction (Figure 17, bottom panel). For consistency, all uncertainty arrays used in this study were produced using our method. To

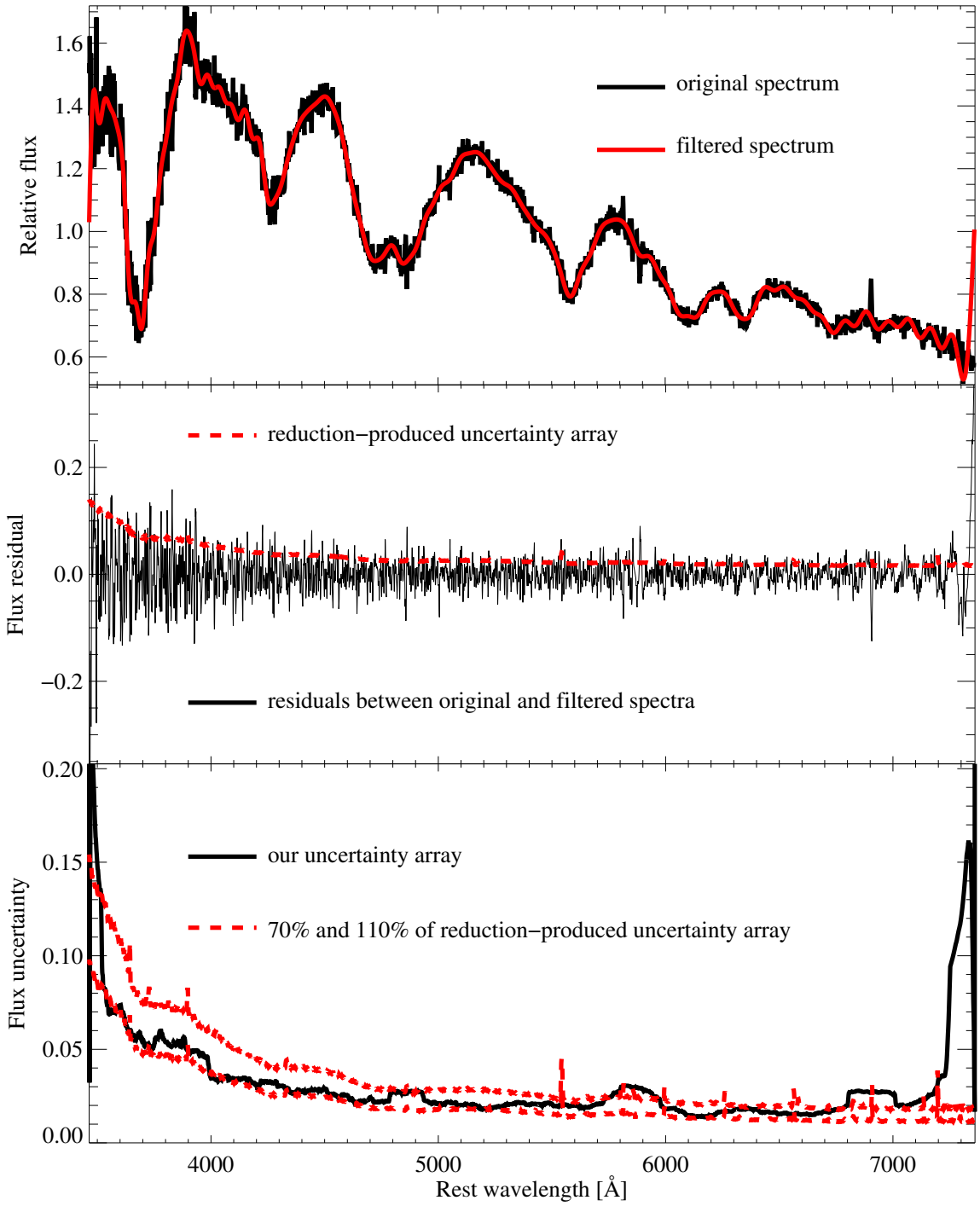

Figure 17. Our uncertainty array, compared to the corresponding reduction-produced uncertainty array. *Top*: spectrum of SN Ib SN 2004gq at $t_{\rm Vmax} = -9$ days (black) and the corresponding Fourier-filtered spectrum (red). *Middle*: residuals between the Fourier-filtered spectrum and the original spectrum (black), i.e., noise in spectrum. For comparison, the reduction-produced uncertainty array (which is the square root of variance spectrum) is shown in red. *Bottom*: our uncertainty array (black) and 70% and 110% of the reduction-produced uncertainty array (red). The high flux variance values at the edges of the wavelength range are due to the edge effect of FT. This will not affect our analysis, since we focus on spectral features that are not at the edges.

ensure the noise derived with our novel method and the Fourier-filtered spectra are reasonable, we visually inspected them as well.

As mentioned earlier, methods to estimate the uncertainty array from a processed spectrum had been developed in the past, but they either require fine tuning on a spectrum by spectrum level, or are automated through the use of parameter choices that are not appropriate for all spectra. Blondin & Tonry (2007) filtered spectra by applying the same bandpass filter to all spectra in Fourier space, but different spectra have different characteristic widths,

especially for different subtypes, that should correspond to different bandpass filters. Blondin et al. (2006) used an inverse-variance-weighted Gaussian filter with the same "smoothing factor" for all spectra in wavelength space. The standard deviation of the Gaussian filter is the product of the wavelength and the "smoothing factor". Thus, the Gaussian filter is wider at longer wavelengths. This accounts for the increased noise at red wavelengths due to the sky emission lines, but it does not take into consideration the fact that the low quantum efficiency at the edges of a CCD will increase the noise at both the blue and the red edges of a spectrum. With our method, each spectrum is filtered with a unique "smoothing factor" that is set by the characteristics of the spectrum itself.

C. THE EFFECT OF SN CONTINUUM ON THE MEASUREMENTS

Ideally, we should measure the velocity and pEW of the SN features themselves, whereas what we actually measured was the velocity and pEW of SN features superimposed on the SN continuum. The continuum should not affect the pEW measurements since it was divided out from the spectra. Since the SN continuum may systematically change the velocity measurements, we checked the effect of SN continuum on velocity measurements by doing the following. We chose a subset of SN spectra and took velocity measurements in both the original spectra and the corresponding continuum-subtracted spectra. Here the continuum is a 13-point cubic spline fit to the corresponding spectrum, the same as that defined in SNID. In principle, the velocity measurements in continuum-subtracted spectra should not be biased by the SN continuum. We found that the differences between the two kinds of velocity measurements are randomly distributed within the error bars from the negative values to the positive values (Section 3.3). Moreover, the benefits of subtracting the SN continuum, e.g., reducing the effect of reddening, are irrelevant for the velocity and pEW measurements. Thus, we measured these quantities in the original spectra, since they are less processed, and thus have less uncertainty compared to their continuum-subtracted counterparts.

D. ROLLING WEIGHTED AVERAGE OF THE MEASUREMENTS

In order to explore bulk properties for different stripped SN subtypes, we calculated rolling weighted averages for each of the various SN properties. The rolling average helps to reduce the bias induced by starting at specific chosen phases, to smooth out short-term fluctuations, and to highlight long-term trends. A cumulative distribution function (CDF) plot of various SN properties or a two-sample Kolmogorov-Smirnov (K-S test) or Anderson-Darling tests (A-D test) on various SN properties would not be appropriate in this study, since the SN properties here evolve with time while the CDF and CDF-based tests cannot treat a two-dimensional dataset well (Babu & Feigelson 2006). The CDF and CDF-based tests can be applied to SN properties within a narrow phase range where the time evolution is ignored, but this does not allow testing for similarities in their evolution. The latter is important in this study given that the SN spectra change significantly in the first one to three months after maximum light.

The rolling weighted average of the measurements in individual spectra is calculated in the following way:

1. We choose a bin size of five days for phases before $t_{\rm Vmax} = 30$ days and of 10 days for later phases. The step size for these bins is one day, i.e., two adjacent bins are $[t_{\rm begin}, t_{\rm end}]$ and $[t_{\rm begin} + 1, t_{\rm end} + 1]$, where $t_{\rm begin}$ and $t_{\rm end}$ are phases in days with respect to the date of maximum light.

2. The weighted-average value of an individual SN in each bin is calculated using all measurements for that individual SN within the bin. The associated error bar is the standard deviation of this average value. Thus, each SN contributes no more than one combined value with an error bar to a bin, which mitigates the impact of a single SN with many data points.

3. Using the above weighted average values of individual SNe, the weighted average value of a SN subtype at a given bin is calculated. The associated error bar is the standard deviation of these weighted average values of individual SNe, which reflects the variation of the measurements in the SNe. If there are fewer than three SNe of the same subtype contributing to the bin, the weighted-average value is meaningless and no value is reported for that bin.